Water Air Soil Pollut (2012) 223:3619–3641
DOI 10.1007/s11270-012-1135-3

Mineralogy and Weathering of Smelter-Derived Spherical Particles in Soils: Implications for the Mobility of Ni and Cu in the Surficial Environment

Sonia Lanteigne · Michael Schindler ·
Andrew M. McDonald · Kristina Skeries ·
Yassir Abdu · Nathalie M. Mantha ·
Mitsuhiro Murayama · Frank C. Hawthorne ·
Michael F. Hochella Jr.

Received: 7 November 2011 / Accepted: 8 March 2012 / Published online: 30 March 2012

Abstract Spherical particles have been sampled from soils and silica-rich rock coatings close to major smelter centers at Coppercliff, Coniston, and Falconbridge in the Sudbury area, Canada. Detailed analyses employing optical microscopy, scanning electron microscopy, transmission electron microscopy, micro-Raman spectroscopy, and Mössbauer spectroscopy have been conducted to elucidate their nature, origin and potential alteration. The spherical particles are on the nano- to millimeter-size range and are composed principally of magnetite, hematite, Fe-silicates (olivine, pyroxenes), heazlewoodite, bornite, pyrrhotite, spinels (including trevorite and cuprospinel), delafossite, and cuprite or tenorite. The spinels present have variable Cu and Ni contents, whereas delafossite and cuprite are Ni free. Texturally, the spherical particles are composed of a Fe-oxide–Fe-silicate matrix with sulfide inclusions. The matrix displays growth features of a Fe-rich phase that commonly form during rapid cooling and transformation processes within smelter and converter facilities. Examination of weathered spherical particles indicates that some sulfide inclusions have dissolved prior to the alteration of the Fe-silicates and oxides and that the weathering of Fe-silicates occurs simultaneously with the transformation of magnetite into hematite. A higher proportion of Cu vs. Ni in the clay and organic fraction noted in the Sudbury soils is explained by (1) the formation of stronger adsorption complexes between Cu and the corresponding surface species and (2) the preferential release of Cu vs. Ni by smelter-derived particles. The latter mechanism is based on the observations that (a) cuprospinels have higher dissolution rates than Ni

---

S. Lanteigne · M. Schindler (✉) · A. M. McDonald ·
N. M. Mantha
Department of Earth Sciences, Laurentian University,
Sudbury, ON P3E 2C6, Canada
e-mail: mschindler@laurentian.ca

K. Skeries
Department of Geological Sciences and Geological
Engineering, Queen's University,
Kingston, ON, Canada

Y. Abdu · F. C. Hawthorne
Department of Geological Sciences,
University of Manitoba,
Winnipeg, Manitoba, Canada

M. Murayama
Department of Materials Science and Engineering,
Virginia Tech,
Blacksburg, VA 24061, USA

M. F. Hochella Jr.
Center for NanoBioEarth, Department of Geosciences,
Virginia Tech,
Blacksburg, VA 24061-0420, USA

spinels, (b) a larger proportion of Cu occurs in the nanometer-size (and thus more soluble) fraction of the emitted particles, and (c) Ni spinels of relatively low solubility form in the alteration zone of heazlewoodite inclusions.

Keywords Soils · Particulates · Heavy metals · Smelter

1 Introduction

Smelting activities are the principal contributors to local and regional atmospheric pollution in the form of metals, metalloids, and sulfur dioxide. Metal(loid)-bearing particles emitted during smelting influence the quality of soil and water systems and have an impact on human health via inhalation of nanometer-size airborne particulate matter (Kalkstein and Greene 1997). Sulfur dioxide emissions from smelters add to global sulfur concentration in the atmosphere and contribute to acidic precipitation, climate forcing, and global pollution (Norman et al. 2004; Bao and Reheis 2003; Hamill et al. 1997; Brock et al. 1995).

Smelters are considered point sources of metal (lloid) pollution where the concentration of emitted elements commonly decreases in surficial environments with distance from the source (Davies 1983). The distribution patterns of elements emitted from point sources have been mapped in soils (e.g., Wren 2012; Hogan and Wotton 1984; Freedman and Hutchinson 1980), peat (e.g., Zoltai 1988), lake sediments (e.g., Jackson 1978), and in humus and till sediments (e.g., Henderson et al. 1998).

The mobility, bioavailability, and toxicity of metals in soils depend on the solubility and reactivity of their host materials (e.g., McNear et al. 2007). Hence, the identification of these metal-bearing hosts is important for risk assessment on the mobility of metals and for the formulation of effective remediation strategies.

This paper represents the first contribution on the mineralogical characterization of metal-bearing phases in soils from the Sudbury area, Canada (Fig. 1a). We focus on the identification of Fe–Ni–Cu-bearing phases in smelter-derived spherical particles and use their weathering characteristics to explain their preferential release of Cu vs. Ni.

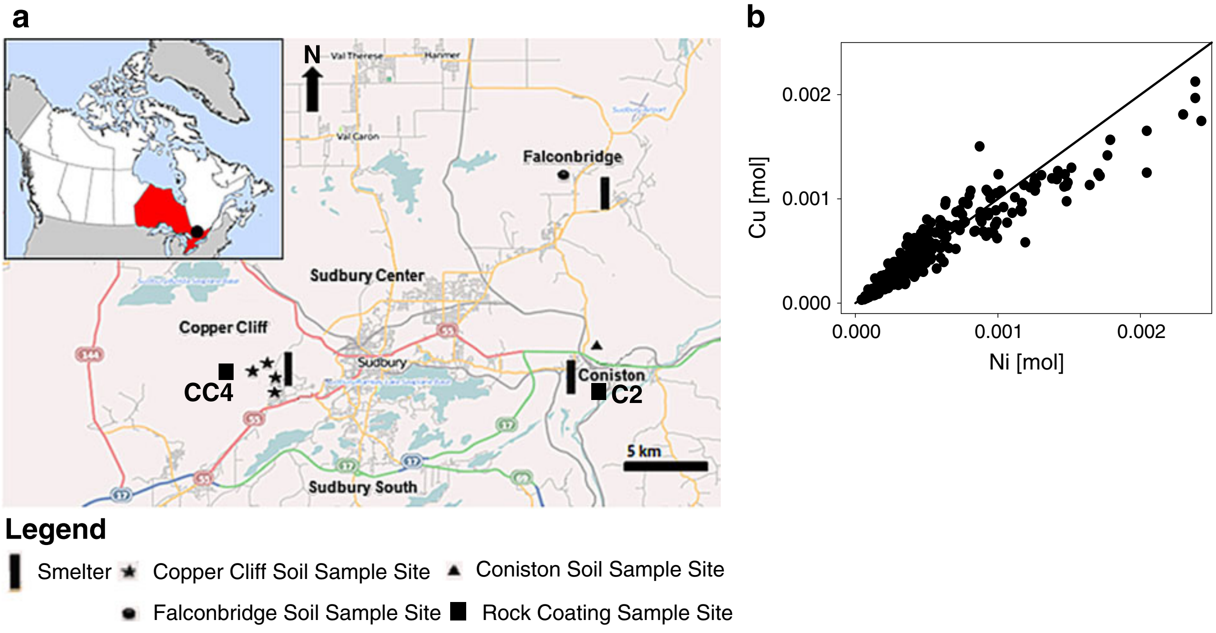

Fig. 1 **a** Map of the Sudbury region with the locations of the sampling sites for the soils (*stars*, *triangle*, *circle*) and silica coatings (*squares*); the smelter areas of Copper Cliff, Coniston, and Falconbridge are indicated with a sketched chimney, and an index in the *upper left corner* shows the location of Sudbury within Ontario, Canada. **b** Plots of the concentrations of Ni vs. Cu in the upper 0–5 cm of the Sudbury soils; plots include data from 275 soil samples and were reported in the Sudbury Regional Soils Study (Wren 2012)

Such data are relevant to understanding the fate and residence time of metals in highly contaminated soils and to developing reclamation strategies for polluted soils in proximity to former and current smelting activities.

1.1 History of Environmental Pollution in the Greater Sudbury Area

In 1886, large Ni–Cu deposits were discovered in the Greater Sudbury area. In 1888, open roast beds and smelters with short emission stacks were erected to process local ore. There were three major smelting centers in the Greater Sudbury area from 1913 to 1972: Copper Cliff, Falconbridge, and Coniston (Fig. 1a, Whitby et al. 1976). During the peak years of emission, these smelters emitted annually on average 1.5 million tons of SO_2, 200 tonnes of Pb, 120 tonnes of As, 50 tonnes of Se, and over 1,000 tonnes of Cu and Ni (Wren 2012; Nriagu and Wong 1983; Ozvacic 1982; Hutchinson and Whitby 1974).

1.2 Former Studies on the Sudbury Soils

In 2001, two comprehensive city-wide soil sampling and analysis studies were carried out to quantify anthropogenic metals in local soils and to determine preindustrial metal levels in local soils. The Sudbury Urban Soil Study (Wren 2012) investigated metal concentrations in local urban soils (e.g., agricultural areas, school yards) and compared these to Ministry of Environment guidelines. The Sudbury Regional Soils Study (SRSS; Wren 2012) analyzed the distribution of metal species in undisturbed soils on a regional scale for three soil depths, 0–5, 5–10, and 10–20 cm. The latter study showed that samples from 0 to 5 cm are generally more enriched in metal(loids) than the layers below and that metal(loid) distribution is consistent with an atmospheric deposition model and the historical industrial activities of the Sudbury area (Wren 2012). Furthermore, the distributions of As, Pb, Cu, Ni and Se follow a NE-SW trending ellipsoid, consistent with the dominant wind directions in the Greater Sudbury area. The concentrations of these metal(loids) drop to background levels at an approximate distance of 120 km from the center of Sudbury (SRSS; Wren 2012). Enrichment factors of elements in the 0–5-cm and in the 10–15-cm layer vs. the corresponding parent material (soil at 80 cm depth from surface) indicate that:

1. As, Pb, Cu, Ni, and Se are derived from an anthropogenic source.
2. The latter elements (Ni, Se) occur in phases of low solubility.
3. Cu, As, and Pb have a higher mobility than Ni and Se within the soil column (SRSS; Wren 2012).

Table 1 lists the concentrations of As, Pb, Cu, Ni, and Se for the depth of 0–5 cm of the soils of the Copper Cliff, Coniston, and Falconbridge areas. Adamo et al. (1996) studied the distribution of Cu and Ni phases in Sudbury soils and showed that Cu is closely associated with clays, organic material, and smelter-derived material, whereas Ni occurs most commonly in smelter-derived particles. Similar conclusions were drawn by the Sudbury soil study to explain an apparent higher mobility of Cu^{2+} relative to Ni^{2+} (SRSS; Wren 2012). The authors of both studies noted that the higher mobility of Cu^{2+} in the Sudbury soils is unusual, because Cu^{2+} commonly becomes less mobile than Ni^{2+} due to the formation of stronger complexes with organic material, Fe–Mn-oxides and clay minerals (Baker 1990).

1.3 Objectives

The historical records on the emission of Cu and Ni indicate that their atomic ratios in the smelter plume varied annually and from stack to stack but were on average close to 1 (SRSS; Wren 2012; Ozvacic 1982; Hutchinson and Whitby 1974). For example, 670 and 500 tons year^{-1} of Cu and Ni were released between 1983 and 1981 from all smelters in the Sudbury area (Ozvacic 1982), corresponding to an atomic Cu/Ni

Table 1 Average chemical composition of the 0–5-cm surface soil (milligram per kilogram dry weight) from the Sudbury Regional Soils Study (Wren 2012) for the regions Coniston, Copper Cliff, and Falconbridge

Location	*n*	Ni	Cu	As	Se	Pb
Coniston	32	265	323	25	2	43
Copper Cliff	21	837	826	29	6	75
Falconbridge	33	283	357	37	3	62

n denotes the number of samples per region ratio of 1.2. Mantha and Schindler (2012) showed that the average atomic ratio between Ni and Cu in the 275 soil samples analyzed in the SRSS is close to 1, indicating that their ratios in the soils have not significantly changed since their atmospheric deposition (Fig. 1b). This suggests that the mobility of Ni and Cu is in fact similar in the soils; however, these elements are associated with different mineral phases. The observed higher accumulation of Cu vs. Ni in clays and organic material can be explained by the formation of stronger adsorption complexes between Cu and the corresponding surface species (Alloway 1990; Baker 1990). However, if similar amounts (in terms of moles) of Ni and Cu were indeed deposited on the Sudbury soils, why and how was Cu preferentially released by smelter-derived particles into the organic and clay fraction of the soils? These questions can be answered by examining in detail the type, composition, and weathering features of Cu- and Ni-bearing phases in the Sudbury soils. Knight and Henderson (2005, 2006) pointed out that smelter particles in soils and humus likely represent many years of emitted particles, whereas particles collected in snow represent only the latest emissions of particles. Hence, the co-existence of different generations of smelter particles in soils can be used to depict weathering sequences for the different phases in these particles. This allows us to determine the alteration sequence of smelter-derived phases and to identify those phases that control the long-term mobility of Cu and Ni in the Sudbury soils.

In this paper, we will examine only smelter-derived spherical particles, because they present the largest group of smelter-emitted particles in the Sudbury soils (there is a very small population of angular Cu and Ni particles <1 %). We identify Fe-, Ni-, and Cu-bearing phases present in weakly and strongly weathered spherical particles and explain the preferential release of Cu vs. Ni using (a) observed weathering features, (b) experimental data on dissolution rates of Cu- and Ni-bearing oxides, and (c) grain-size distributions of spherical particles observed in soils and silica-rich rock coatings.

1.4 Mineralogical Studies on Cu- and Ni-Bearing Particles Emitted by Other Base-Metal Smelters

Notable studies on the mineralogical and chemical composition of particles emitted by other base-metal smelters have been conducted by Knight and Henderson (2005, 2006) and Gregurek et al. (1998, 1999). The former authors examined smelter particles collected in humus around Rouyn-Noranada, Quebec, Canada, and the latter authors characterized particles collected in snow around the Cu–Ni smelters on the Kola Peninsula, Russia. Both studies showed that (a) the majority of smelter-derived particles occur as spherical particles (the industrial term is prills), (b) they formed at high *T* during smelting and converter processes, (c) they possessed distinct internal and external features as a result of their rapid cooling, and (d) they were composed mainly of Fe-silicates and Fe-oxides with minor Fe–Ni–Cu-sulfides.

2 Experimental

Samples of the upper 0–5 cm from acidic soils (pH=4–5) were collected in proximity to former smelters at Copper Cliff, Coniston, and Falconbridge, Sudbury, Canada (Fig. 1a). Sampling sites were at least 100 m from residences, roads, railway tracks, rivers, slopes, and limed areas so as to avoid misrepresenting the soil condition of the area by secondary contamination from sources other than the smelter.

Vegetation, if present, was removed before samples were collected. Magnetic and non-magnetic fractions were separated by running a hand magnet continuously through the bulk soil. The number of spherical particles in the magnetic fraction by far exceeded their number in the non-magnetic fraction (ratio is circa 10:1). Portions of the magnetic fraction were subsequently embedded in epoxy pucks and prepared for optical microscopy, SEM, and Raman spectroscopy.

Samples of silica-rich rock coatings were also collected in the vicinity of the smelters at Copper Cliff (CC), Coniston (C), and Falconbridge (Fig. 1a). Cross-sections of samples from CC and C were embedded into epoxy and subsequently prepared for scanning electron microscopy (SEM) and transmission electron microscopy (TEM) (for more details, see Mantha et al. 2012).

2.1 Scanning Electron Microscopy

Textural and phase analyses of the spherical particles were done with a JEOL 6400 Scanning Electron Microscope operated at 20 kV and a beam current of

1 nA. Particles were examined by backscattered electron (BSE) and secondary electron microscopy and quantitative chemical analysis obtained by energy dispersive X-ray spectrometry (EDS) using the standards SiO_2, albite, MgO, Al_2O_3, K-feldspar, wollastonite, FeS_2, and metallic Fe, Ni, and Cu.

2.2 Focused Ion Beam and Transmission Electron Microscopy

Due to the lack of nanometer-size particles in the soil samples, the grain-size distribution of spherical particles was examined in silica-rich coatings using SEM and TEM. Cross-sections of silica-rich coatings were first coated with gold and palladium to prevent platinum (used in focused ion beam (FIB)) from contaminating the sample. An 8-μm × 20-μm section was removed with a FIB and subsequently lifted using a platinum gas glue. The sections were thinned to electron transparency via ion gas milling (Ga ions) and subsequently mounted on a copper grid. As a result, all energy dispersive analyses (EDS) measure Cu from the grid immediately below the sample. These background levels of Cu were estimated by measuring the Cu $K\alpha$ X-rays emitted from the underlying grid through a hole in the coating sample.

The prepared samples were examined using a FEI Titan 80-300 scanning transmission electron microscope (STEM). The measurements were done at an accelerating voltage of 200 kV in the scanning (STEM, beam diameter approximately 1 nm) and high-resolution modes (HRTEM). Semi-quantitative chemical analyses were obtained using an EDAX r-TEM-EDS system.

2.3 Mössbauer Spectroscopy

The Mössbauer spectra of red-, brown-, and black-colored spherical particles were collected at room temperature (RT). To prepare the Mössbauer absorbers, a number of spheres of each type were embedded on tape and mounted on a Pb disk with a 500-μm aperture. Samples were subsequently measured with a ^{57}Co point source and collected over a velocity range of ±11 mm s^{-1}. The spectra were analyzed using the Voigt-based quadrupole splitting distribution and the hyperfine field distribution methods. The spectrometer was calibrated using the RT spectrum of α-Fe.

2.4 Micro-Raman Spectroscopy

Micro-Raman spectroscopy was done on cross-sections of spheres with various textures and chemical compositions. Spectra were obtained over the range of 50 to 4,000 cm^{-1} and collected in backscattered mode with a HORIBA JobinYvon XPLORA spectrometer interfaced with an Olympus BX 41 microscope, ×100 magnification (estimated spot size of 2 μm), a 1200 grating, and an excitation radiation of 638 nm. Calibration was made using the 521-cm^{-1} line of a silicon wafer.

2.5 X-ray Diffraction

X-ray diffraction was done on selected spheres on the basis of their chemical composition, Raman spectra, and textures. The spheres were extracted from the epoxy using a knife and probe under a binocular microscope and subsequently mounted and centered on a 114.6-mm Gandolfi X-ray diffraction camera. Data were collected using an image-plate system and Cu $K\alpha$ (1.54 Å) radiation. Additionally, powder samples were prepared for soil samples from Copper Cliff, Falconbridge, and Coniston.

Powder and Gandolfi X-ray diffraction measurements were done with a Philips PW 1729 X-ray diffractometer at a voltage and current of 40 kV and 30 mA using Co $K\alpha$ (1.79 Å) and Cu $K\alpha$ radiation (1.54 Å), respectively. Diffraction patterns from powder samples were collected over a scan range of 5–75° 2θ with a step size of 0.02° 2θ and dwell times of 4–10 s.

2.6 Rietveld Refinements

Rietveld refinement was done with Panalytical High Score Plus version 2.2 software. X-ray diffraction peaks were modeled using a pseudo-Voigt profile function with backgrounds being modeled using a six-order polynomial. The zero error, asymmetry (Rietveld), peak shape, and cell parameters were refined for all phases. Preferred orientations of phases were corrected for using the method of Dollase (1986). For minerals present in abundances >5 modal%, atom coordinates and site-occupancy factors (where appropriate) were refined, while the compositions for those phases present in lower abundances were fixed at published values. The quality of the difference between the calculated and observed diffraction profiles was evaluated using standard indices of agreement, the profile R-factor, R_p, the weighted profile R-factor R_{wp}, the expected R-factor, R_{exp}, and the goodness-of-fit index, S. For minerals present in high abundance, the R_{Bragg} index was used as a qualitative guide to the goodness of fit. Relative errors in the modal abundances of the minerals analyzed are functions of concentration: based on the conditions under which the data were collected, for phases present in modal abundances greater than 10 %, the typical relative error is 5 %, with relative errors of 10–15 % for those present in abundances of 5–10 modal%. Relative errors increase rapidly for minerals present in concentrations less than 5 modal%, these typically being on the order of 100 % for minerals present in concentrations below 0.5 modal% (Campbell et al. 2011).

3 Results

The upper 0–5 cm of the soils around the three smelter centers of Copper Cliff, Coniston, and Falconbridge consists of sandy silts with minor clay (the clay fraction was quantified using optical microscopy). They are dominated by quartz and plagioclase and contain minor actinolite, muscovite, and chlorite. Table 2 shows that the mineralogical composition of the soils at the Copper Cliff and Falconbridge smelter areas is similar for plagioclase. Falconbridge contains more quartz and less actinolite and muscovite relative to Copper Cliff. Mineralogical compositions from soils at the Coniston smelter area contain more quartz and less plagioclase. Optical microscopy and SEM indicate that an estimated 5 % of all sand- to silt-size grains in the Copper Cliff soils represents spherical particles, whereas the soils at Falconbridge and Coniston contain less than 2 % spherical particles.

Table 2 Major phases and their modal abundances (modal%) in the soils of the Copper Cliff (CC), Coniston (Co), and Falconbridge (Fal) areas

Phase	CC	Co	Fal
Quartz	50.7	64.7	56.2
Plagioclase	39.4	26.9	39.4
Actinolite	5.3	2.4	1.9
Muscovite	3.5	4.6	0.7
Chlorite	1.1	1.4	1.9

3.1 Chemical and Mineralogical Composition of the Spherical Particles

A total of 104 spherical particles from the magnetic fraction of the soils at Copper Cliff, Coniston, and Falconbridge were examined with SEM-EDS. Many spheres are heterogeneous in composition and morphology and contain areas composed of silicates, (hydr)oxides, sulfides, and sulfates. Chemical analysis of 223 areas indicate that 107 contain significant concentrations of Si (atomic M/Si ratio <10, M = Ca + Mg + Al + Fe), 100 are predominantly composed of (hydr) oxides and sulfates (atomic M/Si ratio >10) and 16 are composed of sulfides (no O) (Fig. 2).

3.1.1 Cu- and Ni-Rich Spherical Particles

Figure 3 displays a ternary diagram with the proportions of Cu, Fe, and Ni from 62 selected analyzed Fe–Ni–Cu-oxides and sulfides. The distribution of the data shows that the majority of the areas are composed of either Fe–Ni-rich oxides or sulfides with minor proportions of Cu [$(\text{Fe, Ni})_{0.8-1.0}\text{Cu}_{0-0.2}$]. Figure 3 also reveals that only sulfides contain similar proportions of Cu, Ni, and Fe, whereas oxides are mainly enriched in two of the three elements (Fe + Cu or Fe + Ni). The latter oxides are divided into three distinct populations: Fe-rich with Fe > Ni + Cu, Fe–Cu-oxides depleted in Ni, and Ni-rich oxides with Ni > Fe + Cu.

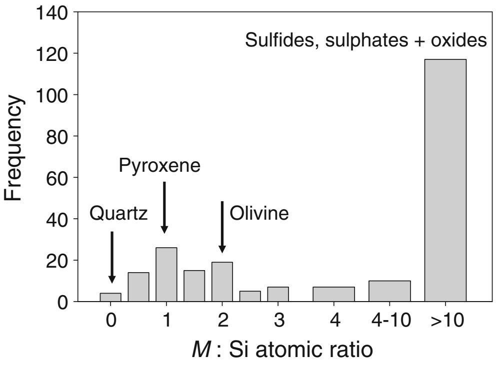

Fig. 2 The frequencies of M/Si ratios (M = Na, Mg, K, Ca, Al, Fe) in areas within the smelter-derived spherical particles, ratios that correspond most likely to silica, olivines, pyroxenes, and sulfide, sulfates, and oxides, are labeled accordingly

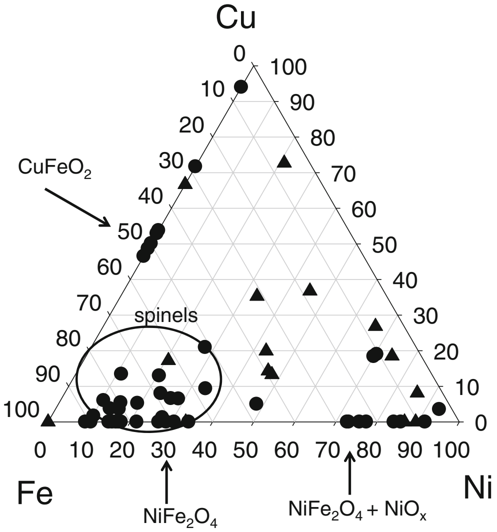

Fig. 3 *Triangular diagram* with the proportions of Fe, Ni, and Cu in areas composed of oxides (*circles*) and sulfides (*triangles*); data points associated with spinels, $NiFe_2O_4$, and $CuFeO_2$ are labeled accordingly

Copper and Ni-rich sulfides occur as inclusions in Fe-oxide–Fe-silicate matrices (Fig. 4a–c), in which the Fe/Si atomic ratio is always greater than 1. All inclusions examined appear to be X-ray amorphous (i.e., they did not produce a diffraction pattern) and were identified via their chemical composition and Raman spectrum. For example, mixtures of heazlewoodite, Ni_3S_2, and bornite Cu_5FeS_4 (Fig. 4a, b), and heazlewoodite and pyrrhotite, $Fe_{1-x}S$ (Fig. 4c), were identified based on observed peaks in the Raman spectra for the sulfide inclusions and the corresponding reference materials.

Panels a and b of Fig. 5 show optical and SEM images of a spherical particle that contains a sulfide inclusion within a Fe-silicate matrix. The inclusion is composed of heazlewoodite and contains small, blue-colored veins enriched in Cu. A Raman spectrum taken from a blue-colored vein and its surroundings indicates the presence of bornite (vein) and heazlewoodite (surroundings, Fig. 5c).

Table 3 lists the observed stretching frequencies for the spectra shown in Figs. 4 and 5, as well as reported frequencies for heazlewoodite and measured standards of bornite and pyrrhotite (from the Sudbury Igneous Complex). Figure 5d shows a ternary diagram with the atomic proportions of Cu, Ni + Fe, and S in all observed sulfide inclusions. The diagram indicates that almost all sulfide inclusions have either *M*/S ratios (*M* = Cu, Ni, Fe) close to 1 or 1.5:1, suggesting the presence of heazlewoodite (1.5:1), bornite (1.5:1), and pyrrhotite (~1:1).

Spheres composed of Fe–Ni–Cu-oxides are either composed entirely of Fe–Ni–Cu spinels or delafossite, $Cu^{+1}Fe^{+3}O_2$ (Fig. 6a, e) or contain rims composed of Fe–Ni–Cu spinels (Fig. 6c, Table 4). The spinels, $X^{2+}Y_2^{3+}O_4$ ($X = Fe^{2+}$, N^{i2+}, Cu^{2+}, $Y = Fe^{3+}$; Fig. 6a, c), are mainly magnetite, Fe_3O_4, Ni- and Cu-bearing magnetite [$(Fe, Ni)Fe_2O_4$, $(Fe, Cu)Fe_2O_4$], trevorite, $NiFe_2O_4$, and cuprospinel $CuFe_2O_4$ (Figs. 3 and 7, Table 4). Numerous spheres also contain Fe–Ni spinel as rims around hollows in their interior (Fig. 6d). These rims have Fe/Ni ratios close to 1, suggesting an intergrowth of trevorite with an unidentified Ni-oxide.

Figure 3 indicates that areas composed of Ni-rich oxides are more abundant than those composed of Cu-rich oxides and that areas composed of spinels with Fe > Ni and Fe > Cu are more abundant than those with Ni ≥ Fe or Cu ≥ Fe. Areas with Cu ≥ Fe are composed mainly of delafossite but can also contain oxides with Cu/Fe ratios of 2:1 and 19.

Mössbauer spectra indicate large proportions of hematite, Fe_2O_3, co-existing with magnetite in the brown- and red-colored spherical particles (Fig. 7a, b). The ratio between the spectral areas for the B-site (Fe^{2+} and Fe^{3+}) and A-site (Fe^{3+}) in magnetite is ~0.8 for brown- and red-colored spheres and ~1.0 for black-colored spheres (Table 5). These values deviate significantly from the theoretical value of ~2, which indicates that the magnetite identified in the spherical particles is non-stoichiometric. This deviation from stoichiometry may result from the partial oxidation of Fe^{2+} to Fe^{3+} and/or partial substitution of divalent cations, e.g., Ni^{2+}, for Fe^{2+} at the octahedral B-sites (Morris et al. 2004). Optical microscopy, SEM, and Raman spectra indicate that hematite occurs mainly in rims of strongly weathered spherical particles (Fig. 7a, b). These rims are commonly depleted in Cu and Ni with respect to magnetite.

3.1.2 Fe-Oxide–Silicates

The majority of the Si-rich areas have *M*/Si ratios of 1:1 and 2:1 (*M* = Na, Mg, K, Ca, Al, Fe; Fig. 2), suggesting the occurrence of pyroxene ($M^{2+}SiO_3$) and olivine group ($M^{2+}{}_2SiO_4$) minerals. Micro-Raman and

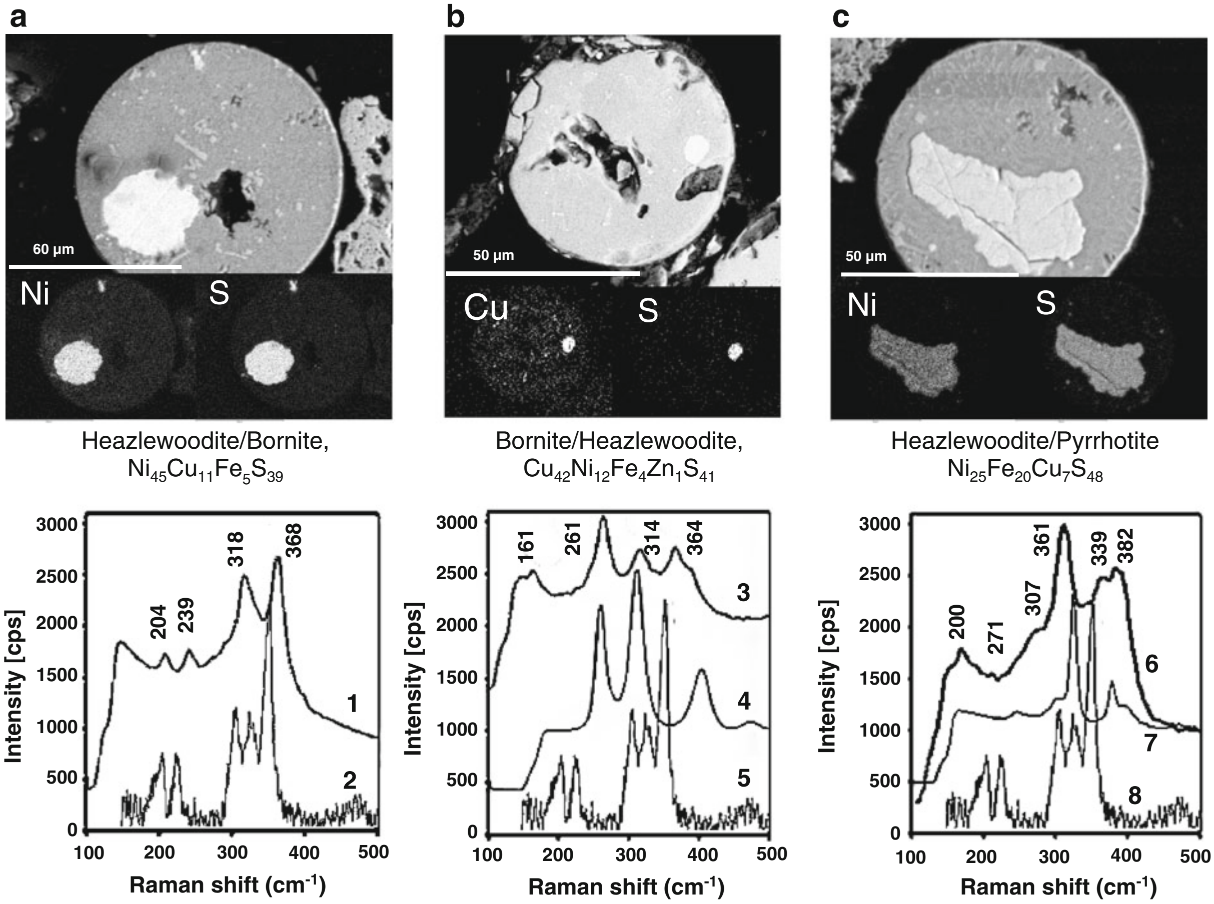

Fig. 4 SEM images (in BSE mode), distribution maps for Ni, Cu, and S, and Raman spectra for **a** a heazlewoodite/bornite inclusion with Ni > Cu; **b** a bornite/heazlewoodite inclusion with Cu > Ni; and **c** a heazlewoodite/pyrrhotite inclusion with Fe ~ Ni; the Raman spectra are numbered as follows: *1* heazlewoodite in sulfide inclusion, *2* heazlewoodite reference spectrum (Cheng et al. 2007), *3* bornite/heazlewoodite in sulfide inclusion, *4* bornite reference spectrum (this study), *5* heazlewoodite reference spectrum (Cheng et al. 2007), *6* heazlewoodite/pyrrhotite in sulfide inclusion, *7* pyrrhotite reference spectrum (this study), *7* heazlewoodite reference spectrum (Cheng et al. 2007)

XRD methods could not be used to unequivocally identify the silicates. However, the Mössbauer spectrum of the black-colored spheres (Fig. 7d) indicates the presence of $^{[6]}Fe^{2+}$ and $^{[6]}Fe^{3+}$ components ($^{[6]}Fe^{2+}$: CS=0.98, QS=2.2; $^{[6]}Fe^{3+}$: CS=0.42, QS=0.97; Table 5), which have CS and QS values consistent with those reported for hedenbergite, $CaFeSiO_6$ ($^{[6]}Fe^{2+}$: CS=1.19, QS=2.22), and Fe^{3+}-bearing diopside ($CaMg_{0.9}Fe_{0.2}Si_{1.9}O_6$, $^{[6]}Fe^{3+}$: CS=0.43, QS=1.07; McCammon 1995 and references therein).

Many spherical particles with mixtures of Fe-silicates and Fe-oxides display distinct internal textures suggesting formation at high *T*. These textures can be easily distinguished from weathering features by the absence of dissolution features and secondary precipitates such as sulfates and hematite. The most common textures are:

(a) Dendritic: containing Fe-oxide dendrites in a silicate matrix with Fe/Si ratios commonly lower than 1 (Fig. 8a)
(b) Skeletal: containing Fe-oxide crystals in a silicate matrix with Fe/Si ratios always lower than 1 (Fig. 8b)
(c) Tabular: containing crystals of magnetite in a silicate matrix with Fe/Si ratios commonly close to 1 (Fig. 8c)
(d) Porphyritic: containing large crystals of magnetite in a silicate matrix with Fe/Si ratios commonly less than 0.4 (Fig. 8d)

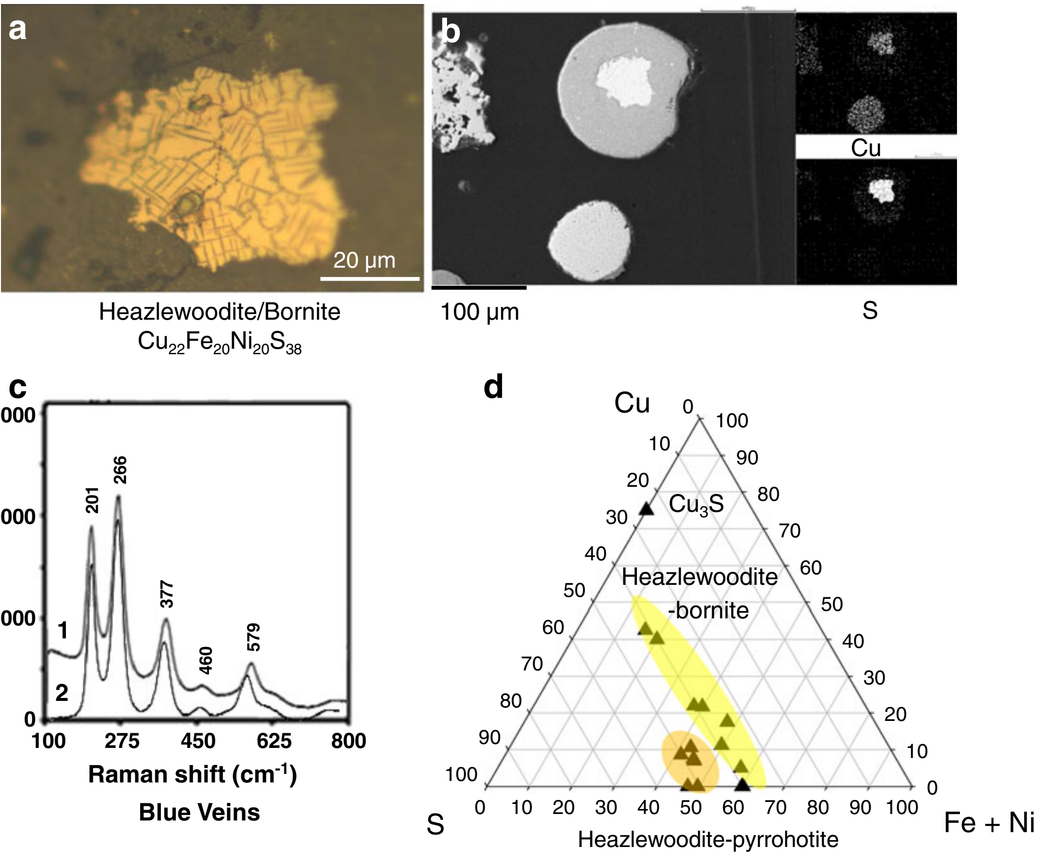

Fig. 5 **a** Optical image in reflection mode of a heazlewoodite inclusion with micrometer-size bluish veins of bornite, **b** corresponding SEM image with the distribution maps for Cu and S, and **c** Raman spectra from *1* the center of the bluish veins and *2* a bornite reference compound (this study); **d** *triangular diagram* with the proportion of S, Fe + Ni, and Cu in the heazlewoodite–bornite (*marked in yellow*) and heazlewoodite–pyrrhotite (*marked in orange*) assemblages

3.2 Size Variations of the Spherical Particles

Optical microscopic and SEM studies indicate that spherical particles in Sudbury soils range in diameter from 1–2 µm up to 2 mm. The apparent absence of spherical particles with diameters in the upper nanometer range (100–1,000 nm) may be the result of both their low proportions and their

Table 3 Observed vibrational stretching frequencies (per centimeter) in Fe–Cu–Ni-sulfides

Phase	Observed vibrational stretching frequencies (cm^{-1})										References
Heazlewoodite (standard)				350	325	304		224	202	188	Cheng et al. (2007)
Heazlewoodite (calculated)				367	320	317		241	204	201	Wang et al. (2007)
Heazlewoodite–bornite, $Fe_5Ni_{45}Cu_{11}S_{39}$ (Fig. 4a)				368		318		239	204		
Ni matte (Fig. 10b)				351	323	304		221	196	187	
Bornite (standard)	784	579	464	377			266		201		This study
Bornite–heazlewoodite, $Fe_4Ni_{12}Cu_{42}Zn_1S_{41}$ (Fig. 4b)				364	314		262			161	
Heazlewoodite–bornite, $Fe_{20}Ni_{20}Cu_{22}S_{38}$ blue veins (Fig. 5b)		568	457	359			266		201		
Pyrrhotite (standard)		400	371			310	285		214		This study
Heazlewoodite–pyrrhotite, $Fe_{20}Ni_{25}Cu_7S_{48}$ (Fig. 4c)			382	361	339	307	271		200		

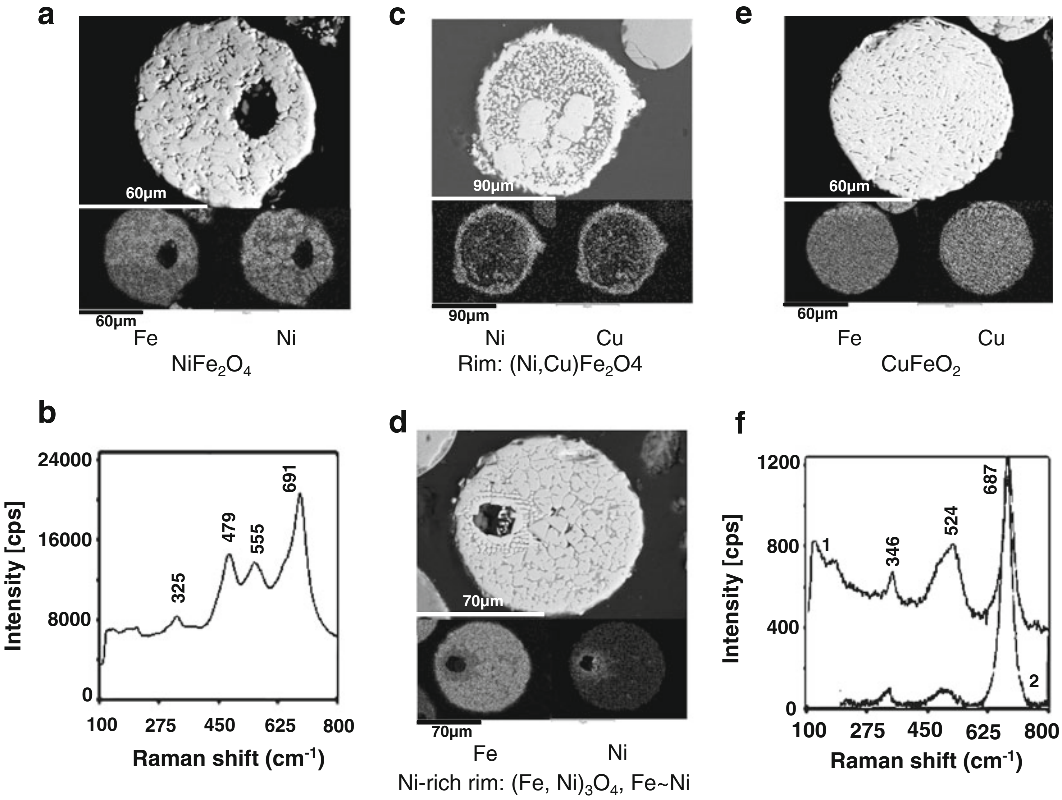

Fig. 6 SEM images (BSE mode), distribution maps for Fe, Cu, and Ni, and Raman spectra for spheres composed of **a**, **b** trevorite, $NiFe_2O_4$; **c** trevorite and cuprospinel, (Ni, Cu)Fe_2O_4; **d** trevorite and an unknown Ni-phase; and **e**, **f** delafossite, $CuFeO_2$ (*1*) and a delafossite reference compound (*2*) (Pavunny et al. 2010)

preferential removal during preparation of epoxy pucks.

Mantha et al. (2012) showed that acidic fumigation and rain enhances the chemical weathering rate of exposed rocks in the Sudbury area. Non-stoichiometric dissolution of silicate minerals under these acidic conditions resulted in the formation of a silica-gel-type coating, which in turn promoted the uptake and

Table 4 Observed vibrational stretching frequencies (per centimeter) in Fe–Cu–Ni-oxides phases

Phase	Observed vibrational stretching frequencies (cm^{-1})					References
Magnetite (standard)	663–676	530–555	418–420	319–320		De Faria et al. (1997)[a]
$NiFe_2O_4$ nanoparticles (standard)	690 (10)	580 (10)	490 (10)	330 (10)		Ahlawat and Sathe (2010)
$(Fe, Ni)_3O_4$ (Fig. 6a, b)	691	555	479	325		
$(Cu, Ni)Fe_2O_4$ (Fig. 6c)	672	532	456	309		
Ni-rich rim $(Fe, Ni)_3O_4$ (Fig. 6d)	666	540	465	309		
Delafossite (standard)	690		515	352		Pavunny et al. (2010)
Delafossite $CuFeO_2$ (Fig. 6f)	686		519	346		
Hematite (standard)		604 (8)	495 (2)	400 (8)	288 (5)	De Faria et al. (1997)[a]
Hematite rim (Fig. 7b)		582	482	389	274	

Note that errors are given for frequencies where the shift in frequency was monitored with the change in laser power

[a] Range of observed frequencies

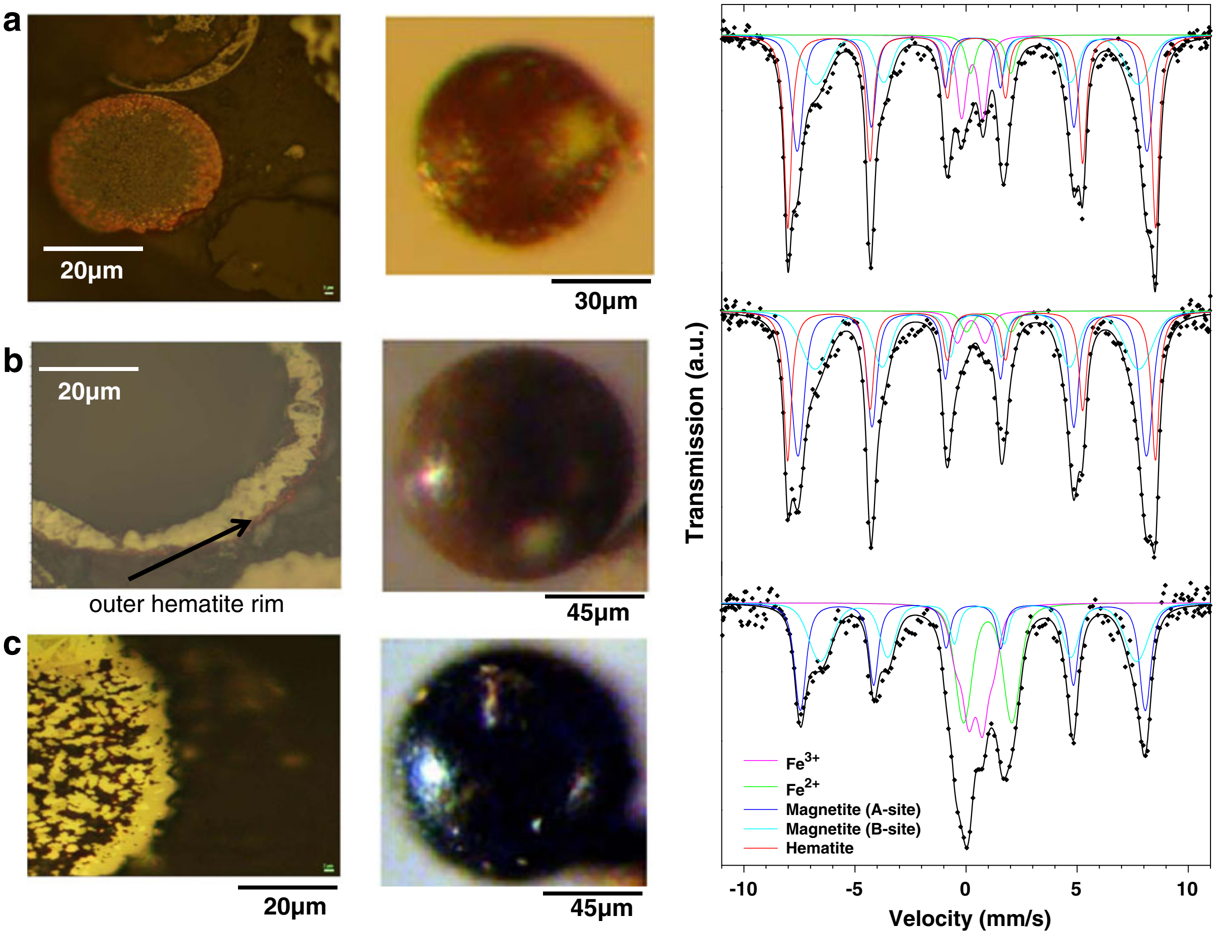

Fig. 7 Optical images of cross-sectioned spherical particles in reflection mode under cross-polarized light (*left*), optical images of red-, brown-, and black-colored spheres (*center*), and the corresponding Mössbauer spectra (*right*) with the fitted components for hematite (*red line*), magnetite (*light and dark blue line*), and unknown Fe^{2+}- (*green line*) and Fe^{3+}-silicates (*pink*): **a** red-colored spherical particles with a large proportion of hematite visible in the outer rim; note that the red-colored sphere on the left is not identical with the sphere shown in the center; **b** brown-colored spherical particles with a smaller proportion of hematite, visible as a thin layer in the outer rim; **c** black-colored spherical particles without any hematite

preservation of smelter-derived nano- to micro-size particulates (Durocher and Schindler 2011; Mantha et al. 2012; Schindler et al. 2009, 2010). The preservation of nanometer-size spherical particles in these rock coatings permits examination of the textures and chemical compositions of the finer (and thus, more soluble) fraction of spherical particles.

TEM and SEM studies on sections of the coating samples indicate the presence of nano- to micrometer-size spherical particles in a silica-rich matrix (Fig. 9). Similar to their counterparts in the soils, the micrometer-size spheres are composed of Fe-oxides and Fe-silicates. They display distinct internal textures, including cross-hatched patterns of skeletal Fe-oxide crystals in Fe-silicate matrices (Fig. 9b) or Ni-rich rims around more or less homogenous Fe-silicate matrices (Fig. 9c). Nanometer-size spheres in these coatings are composed of Cu–Fe–Ni-rich spinels (Fig. 9d, e) and Cu-oxides (Fig. 9f), consisting with the presence of magnetite, trevorite, cuprospinel, and tenorite (CuO) or cuprite (Cu_2O) (note that no electron diffraction pattern was taken from the spheres in Fig. 9f). Chemical analysis of over 30 spherical particles indicates that Ni occurs predominantly in spheres of the micrometer-size fraction, whereas Cu is mainly present in spheres of the nanometer-size fraction (i.e., the ratio between the number of Cu- and Ni-bearing nanometer-size spherical particles is circa 5:1).

Table 5 Results from the Mössbauer spectroscopy: fitted components which can be either a phase or a crystallographic site containing Fe, their center shift relative to α-Fe at room temperatures (CS), their quadrupole splitting for a paramagnetic doublet (or the quadrupole shift for a magnetic pattern, QS), their hyperfine magnetic field (*H*), and their relative area in the spectra for spheres of different colors

Sample	Phase or Fe site	CS (mm s^{-1})	QS (mm s^{-1})	*H* (T)	*A* (%)
Red- and orange-colored spheres	Hematite	0.36 (1)	−0.10 (1)	51.3 (1)	35 (4)
	Magnetite (A-site)	0.28 (3)	−0.01 (2)	48.8 (3)	29 (4)
	Magnetite (B-site)	0.49 (6)	0	44.9 (8)	23 (4)
	Fe^{2+} in silicate	1.1 (1)	1.8 (2)	–	4 (2)
	Fe^{3+} in silicate	0.29 (6)	1.0 (1)	–	9 (1)
Brown-colored spheres	Hematite	0.36 (1)	−0.11 (1)	51.3 (1)	28 (4)
	Magnetite (A-site)	0.29 (1)	−0.02 (1)	48.6 (1)	38 (4)
	Magnetite (B-site)	0.47 (4)	0.02 (3)	45.2 (4)	28 (4)
	Fe^{2+} in silicate	1.03 (6)	2.01 (7)	–	2 (1)
	Fe^{3+} in silicate	0.23 (5)	1.25 (6)	–	4 (1)
Black-colored spheres	Magnetite (A-site)	0.32 (3)	−0.02 (2)	48.1 (2)	29 (4)
	Magnetite (B-site)	0.58 (6)	−0.02 (4)	44.1 (5)	28 (4)
	Fe^{2+} in silicate	0.98 (5)	2.2 (1)	–	22 (3)
	Fe^{3+} in silicate	0.42 (5)	0.97 (5)	–	21 (3)

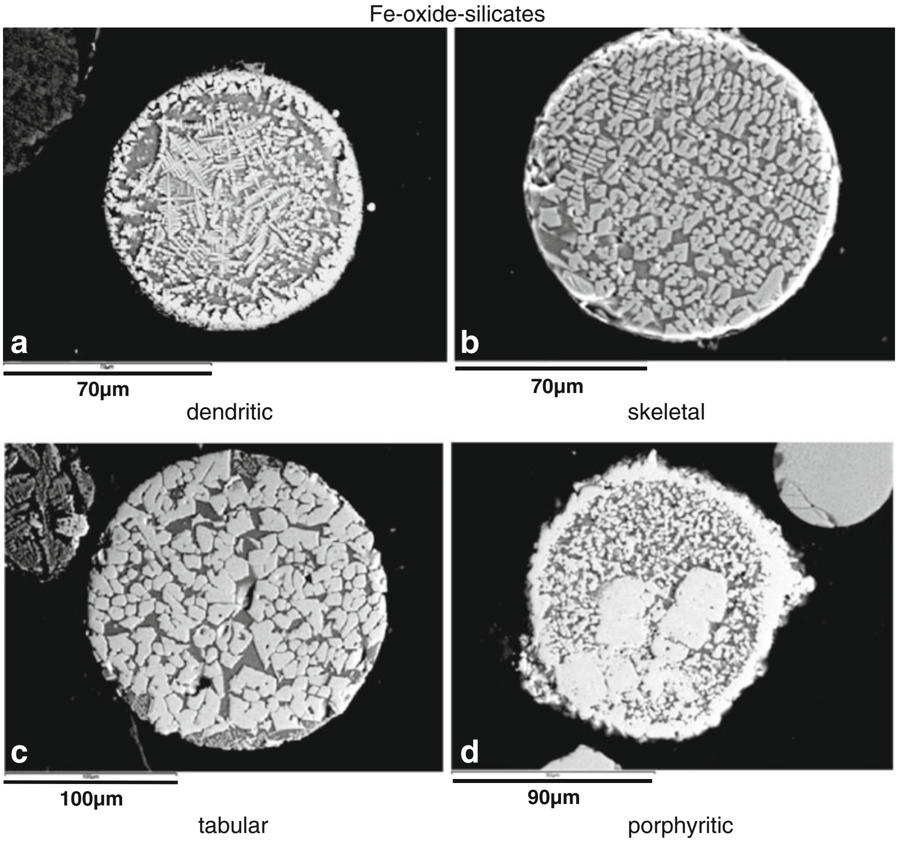

Fig. 8 **a**–**d** Most common observed textures in spherical particles composed of mainly Fe-oxide and Fe-silicates

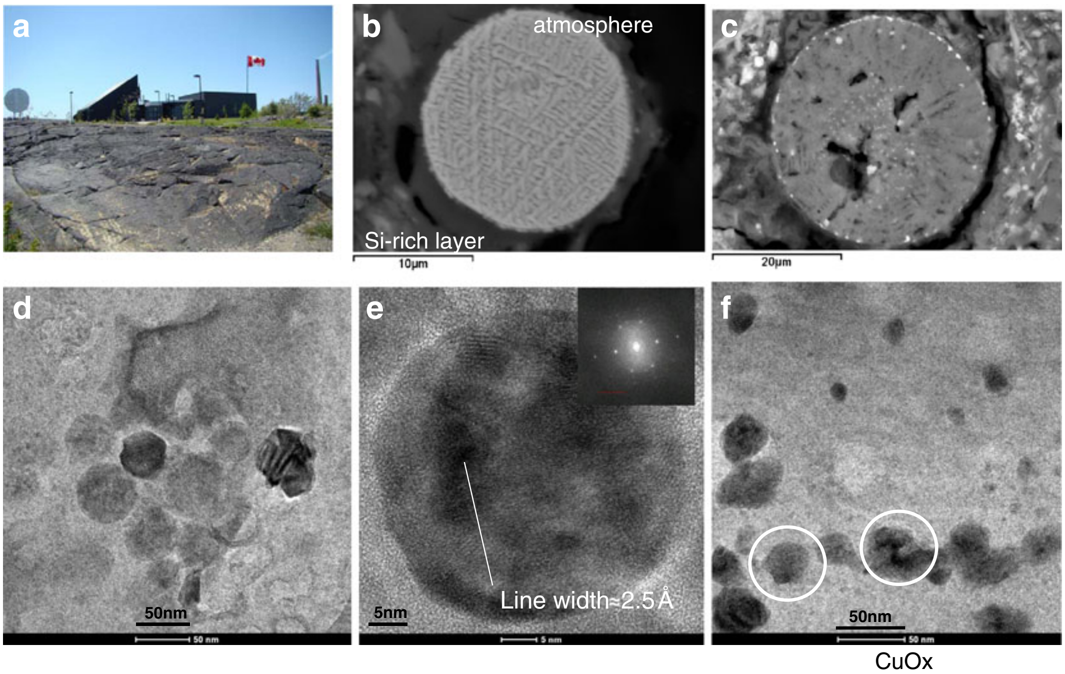

Fig. 9 **a** The black rock coating of the Sudbury area on exposed rocks; **b**, **c** BSE images of micrometer-size smelter-derived spherical particle in a coating from Copper Cliff; **d**, **f** HRTEM images and FFT patterns of former atmospheric nanoparticles within the amorphous silica matrix of the coatings: **d** clusters of nanometer-size Fe-rich spheres; **e** HRTEM and FFT patterns of a nanometer-size Fe-rich spherical particle with spinel-type structure; the typical lattice fringe distance of 2.5 Å for $d_{(310)}$ is indicated with the width of a *white line*; **f** cluster of angular to spherical CuO_x nanoparticles

4 Discussion

The spherical particles are composed mainly of magnetite and Fe-silicates, but also contain Cu- and Ni-rich phases such as trevorite, cuprospinel, delafossite, heazlewoodite, and bornite. The occurrence and chemical composition of these phases can be understood only if one considers the origin and formation of the spherical particles, as well as the structures of the Cu–Ni-bearing phases. The stability of the Cu- and Ni-rich phases can be evaluated when one inspects the morphology of weathered spherical particles and considers both the formation of secondary alteration products and dissolution studies on synthetic analogues.

4.1 Overview of the Ore Refinement Processes at Copper Cliff

The major Cu- and Ni-ore minerals in the Sudbury area are chalcopyrite, $CuFeS_2$, and pentlandite, $(Fe,Ni)_9S_8$, with minor amounts of cubanite, $CuFe_2S_3$, bornite, Cu_5FeS_4, and millerite, NiS. At the Copper Cliff facility, these Cu- and Ni-sulfides are separated via a floatation process, yielding concentrates of Ni- and Cu-sulfides. These concentrates are subsequently smelted at different temperatures, creating a Cu- and Ni-sulfide-rich matte and a slag composed of mainly magnetite, fayalite, or SiO_2. Sulfur dioxide evolved in this stage is directed to an acid plant to produce H_2SO_4 (Pengfu and Chuanfu 1997). In the subsequent converting processes, the remaining Fe and S are driven from the molten matte by O_2-enriched air into the matte. In the final steps, Cu- and Ni-rich matte undergoes chemical or electrochemical refining processes.

4.2 Emission and Transformation of Spherical Particles in the Smelter, Converter, and Atmosphere

Emissions produced during smelting and converter processes commonly consist of SO_2, droplets of slag and matte, unreacted flux, condensed particles, and finer sulfate-bearing aerosols, all of which were released without any filtering in the past. High percentages of these gases are now cooled in acidic plants or electrostatic precipitators, which dramatically reduce the emission of SO_2 and metal-bearing particular matter (Wren 2012).

Smelter and converter gases commonly leave the corresponding facilities at $T > 1,200$ °C and are quench-cooled in air within seconds to several hundred degrees Celsius. For example, Evans et al. (1991) showed that gases leaving the Horne Cu smelter reactor at Rouyn-Noranda at 1,230 °C were quench-cooled to 620 °C in 0.6 s and further cooled down to 350 °C in 6 s.

Particulate matter in the emissions originates either from vaporization and condensation of gaseous components or through the collision of solid and liquid particles (Samuelsson and Bjorkman 1998). These particulates commonly transform during the smelting, cooling, and filtering processes before they are emitted to the atmosphere. In the latter medium, finer particulate matter and especially sulfur-bearing aerosols can oxidize and interact with atmospheric components (Batonneau et al. 2004). These processes lead to a wide variation in size, chemical and mineralogical composition, as well as internal and external morphologies of emitted particulate matter and finer aerosols (Knight and Henderson 2005, 2006; Kliza et al. 2000; Gregurek et al. 1998, 1999; Lastra-Quintero 1998; Samuelsson and Bjorkman 1998; Adamo et al. 1996; Chan et al. 1982).

4.3 Internal (Non-weathered) Textures of the Spherical Particles

Knight and Henderson (2005, 2006) and Gregurek et al. (1998, 1999) provided detailed descriptions of the internal morphology of smelter-derived spherical particles in humus around Rouyn-Noranda, Quebec, and in snow samples around the Ni–Cu smelter on the Kola Peninsula, respectively. Knight and Henderson (2005) further classified internal and external textures of spheres from Rouyn-Noranda and deduced the conditions of formation for each group.

Comparing the internal textures of non-weathered to weakly weathered spherical particles in Sudbury soils with those observed at Rouyn-Noranda and the Kola Peninsula indicates (a) the absence of prominent sulfide inclusions in particles from Rouyn-Noranda and (b) similar textures in spherical particles composed of Fe-oxides and Fe-silicates. For example, Fe-oxide–silicate spheres with a platy (Fig. 6a) or dendritic texture (Fig. 8a) have also been observed at Rouyn-Noranda and on the Kola Peninsula.

The textures shown in Fig. 6 represent growth features of a Fe-rich phase (mainly spinel but also possibly olivine group minerals) that formed during rapid cooling and transformation processes within the smelter and converter facilities. The growth of a phase in a melt is controlled mainly by the growth rate Y and the diffusion coefficient of the rate-controlling species in the melt, D (Kirkpatrick 1975). In the case of homogenous nucleation, the ratio D/Y is large at small undercooling and allows the formation of euhedral crystals. An increase in undercooling results in a decrease of the ratio D/Y and thus in the formation of skeletal, dendritic, and spherulitic growth features (Lofgren 1974). In the case of heterogenous nucleation, formation of growth features depends on the number of induced seeds, the temperature during seed inducement, and to a lesser extent, on the type of seeds. For example, Connolly and Hewins (1995) injected dust particles into melt droplets to simulate the growth features observed in chondrules. They found larger growth rates and thus more skeletal to dendritic growth features, when injecting either a higher number of dust particles (high values of Y) or when injecting dust at lower T (higher degree of undercooling and lower values of D). Hence, the occurrence of dendritic and skeletal textures (Fig. 8a, b) vs. tabular and porphyritic features (Fig. 8c, d) indicates either higher degrees of undercooling, higher numbers of injected dust particles, or lower temperatures during the trapping of smaller dust particles by molten droplets of slag, matte, and unreacted flux.

Connolly and Hewins (1995) also showed that the collision of dust particles with molten droplets at temperatures close to 1,000 °C produced rims of particles on each sphere. This feature has been observed on spheres in soils (Fig. 8d) and coatings (Fig. 9c). There is also the possibility that these rims were formed through dissolution–reprecipitation processes on the surface of these particles. However, Mantha et al. (2012) showed that spherical particles in the coatings are well-preserved by a silica-rich matrix and rarely display any weathering features. This observation indicates that the observed Cu- and Ni-rich rims on spherical particles in the coatings likely formed through trapping of finer dust particles by molten droplets of lower viscosity and suggests that similar rims on spherical particles in the Sudbury soils were also formed through dust–molten droplet collisions.

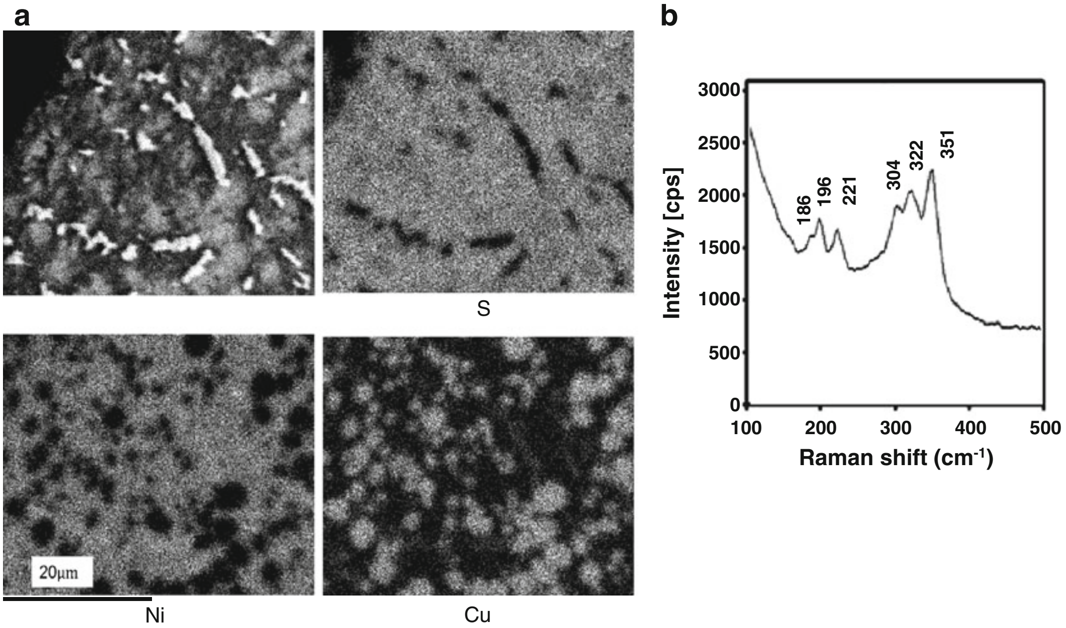

Fig. 10 **a** SEM (BSE mode) and chemical distribution maps for S, Ni, and Cu in a Ni matte from the Falconbridge smelter facility; **b** Raman spectrum taken from the Ni-rich parts of the Ni matte

4.4 Occurrence and Chemical Composition of the Fe–Ni–Cu-Sulfides

Ore and Cu- and Ni-rich matte are the major sources of molten sulfide droplets in the gas phase formed during smelter and converter processes. Heazlewoodite is the major phase in the Ni matte (e.g., Thyse et al. 2011; Ertseva et al. 2003; Dutrizac and Chen 1987). Depending on the concentrations of Cu and Fe, it commonly occurs with chalcocite, Cu_2S, a Cu–Ni alloy, bornite and minor phases such as metallic Cu and Ni and Fe–Cu–Ni-oxides (Ertseva et al. 2003; Dutrizac and Chen 1987). Heazlewoodite, chalcocite, and the Cu–Ni alloy can exhibit intergrowths on the micrometer and nanometer scales, and the proportions of the major phases (e.g., chalcocite and heazlewoodite) can be estimated *via* the ratio between the metals (Ni + Cu) and S (Dutrizac and Chen 1987).

Figure 10a shows a BSE image and distribution maps for Cu, Ni, and S in Ni matte from the Falconbridge smelter facility. Figure 10b shows a Raman spectrum taken from a Ni-rich area of the Ni matte and Table 3 lists the corresponding stretching frequencies. Distribution maps, XRD patterns, and Raman spectra indicate (a) the occurrence of heazlewoodite, chalcocite, and an alloy, the latter with an average composition of $CuNi_3$; (b) low concentrations of Fe (<1 wt%); (c) low concentrations of Cu in areas composed of mainly heazlewoodite (<5 wt%); and (d) and an absence of pyrrhotite and bornite. The latter observation is in agreement with studies by Ertseva et al. (2003) and Dutrizac and Chen (1987) who showed that heazlewoodite in Ni matte accommodates only minor amounts of Cu (around 2 wt%).

In comparison, the sulfide inclusions in the spherical particles of the Sudbury soils are composed mainly of heazlewoodite, bornite, and pyrrhotite, whereas chalcocite and Cu–Ni alloys may only occur in low to undetectable proportions. Similar to the Ni matte, heazlewoodite is intergrown with Cu-rich phases such as bornite or chalcocite. Conversely, inclusions composed of mainly heazlewoodite contain higher concentrations of Fe (>3 wt%) than the Ni matte (this study; Dutrizac and Chen 1987). The discrepancy between the chemical composition of Ni matte and the heazlewoodite inclusions may be explained by:

(a) A decrease in the Fe concentration of the Ni matte through improvements in the smelter and converter techniques

(b) Release of Fe–Ni–Cu-sulfide droplets into the gas phase during smelter and converter processes

(c) Interaction of Ni–Cu-sulfide droplets with either the surrounding Fe-oxide–silicate shell or with Fe-sulfide droplets and the subsequent transformation of chalcocite into bornite

4.5 Occurrence and Chemical Composition of the Fe–Ni–Cu-Oxides

Slag, ore, and oxidized parts of the matte are the major sources for oxides in the gas phase of a smelter and converter facility. Magnetite is the most common oxide in slag produced by the smelting of Cu- and Ni-rich ores. Here, it occurs in association with other spinels such as trevorite, cuprospinel, and Cu-oxides such as delafossite and cuprite (e.g., Vitkova et al. 2010; Gbor et al. 2000).

Trevorite, cuprospinel, and delafossite are the most common Cu–Ni-oxides observed in the spherical particles of this study. The former two minerals have an inverted spinel structure with Cu and Ni in octahedral coordination. However, Dural (2009) showed that quenching of $CuFeO_2$ melts results in the formation of cubic $CuFe_2O_4$, where Cu^{2+} occurs at both the octahedral and tetrahedral sites. Similarly, McNear et al. (2007) showed that Ni^{2+} can have an average coordination number of [5] in some trevorite samples. Furthermore, Tang et al. (1989) showed that rapid cooling of $CuFe_2O_4$ samples from $T>750$ °C leads to the formation of O-deficient Cu spinels through the partial reduction of Cu^{2+} to Cu^{+}.

Copper (I) is also present in delafossite, $Cu^{+}Fe^{3+}O_2$, and cuprite, Cu_2O, where it occurs in linear coordination. Nickel (II) most commonly occurs in octahedral coordination with O and therefore does not replace Cu^{+} in delafossite or cuprite. Nickel (II) may replace Fe^{3+} in delafossite (in octahedral coordination), but this would require a coupled substitution where another divalent cation (M^{2+}) must replace Cu^{+}:

$$Cu^{+} + Fe^{3+} \leftrightarrow M^{2+} + Ni^{2+} \quad (1)$$

There are no divalent cations that can occur in linear coordination with O. Hence, Ni^{2+} or another divalent cation cannot be incorporated into the structures of delafossite or cuprite, thus explaining that these minerals are Ni-deficient (<1 at.%) relative to those with the spinel structure.

4.6 Weathering Features and Products

Figure 11 displays a proposed weathering sequence of spherical particles with a sulfide inclusion, for which further evidence will be provided in the proceeding text. Note that the selected spherical particles do not necessarily contain the same sulfide or Fe-oxide–silicate texture.

Initially, a spherical particle occurs with unaltered sulfides (heazlewoodite/bornite). In step 2, the sulfide inclusion (heazlewoodite) becomes exposed to the atmosphere and pore water through fractures within the surrounding matrix (magnetite–Fe-silicate) and begins to oxidize, resulting in the formation of a Ni-bearing Fe-(hydr)oxide rim.

The third step involves the removal of $(SO_4)^{2-}$ from the interior of the sphere. With a rapid removal rate of the anion, Ni^{2+} may precipitate as a hydroxide in the surroundings of the inclusion, which, upon aging, can transform into Ni-bearing oxides (step 3a). This conclusion agrees with observations by Cornell et al. (1992) that trevorite forms through transformation of Ni-bearing Fe-hydroxides into thermodynamically more stable crystalline phases such as goethite and magnetite. At a low removal rate of $(SO_4)^{2-}$, the sulfide inclusion may be replaced by a sulfate (Fe-sulfate with minor amounts of Ni, K, and Al) as depicted in image 3b of Fig. 11. The image also shows that at this stage, the Fe-silicate matrix begins to alter and secondary Ca–Al–Fe-silicates form on the outer rim of the spherical particle, whereas the magnetite crystals remain unaltered (Fig. 11).

In step 4, the sulfide–sulfate inclusion is completely removed, and the weathering of the silicates creates gaps between the silicate matrix and a magnetite–hematite rim. In step 5, the gaps between the magnetite–hematite rim and the silicate matrix increase, and numerous fractures and etch pits form within the silicate matrix. In step 6, the silicate matrix completely dissolves, leaving a magnetite–hematite rim which subsequently collapses in step 7.

Figure 12 shows a proposed weathering sequence for spherical particles with an angular texture of magnetite within a Fe-silicate matrix. In the first step, there is an unaltered or weakly weathered spherical particle. In step 2, the silicate matrix strongly alters and both etch pits and grooves form on the surface of the magnetite crystals. In step 3, the silicate matrix is completely dissolved and parts of the magnetite–

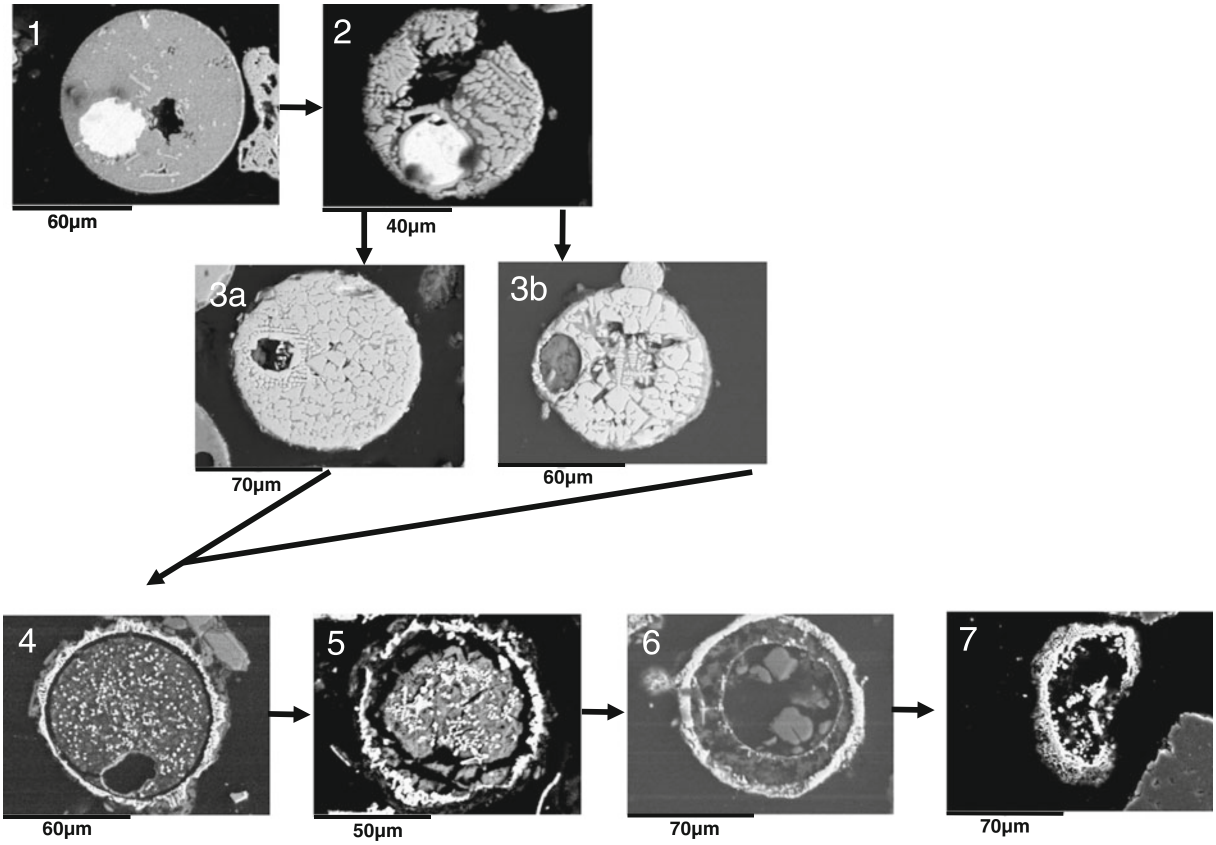

Fig. 11 Proposed weathering sequence (*1*–*7*) for smelter-derived spherical particles with a sulfide inclusion (see text for details). The occurrence of trevorite in 3a is shown as a white rim around the hole on the left side

hematite skeleton are removed. In the next step, the magnetite–hematite skeleton collapses as depicted in step 7 of Fig. 11.

4.7 Other Potential Weathering Products

The types of soil and soil treatment have a pronounced effect on the speciation of metals in the soil (e.g., McNear et al. 2007). Portions of the acidic soil in the Sudbury area has been limed (Wren 2012) and the weathering of Cu- and Ni-bearing spherical particles in these soils likely differs from those in acidic soils, due to higher and lower activities of $(CO_3)^{2-}$ and H^+, respectively. Potential Cu- and Ni-bearing phases present in alteration rims around heazlewoodite, chalcocite, delafossite, and Cu- and Ni-rich spinels can be narrowed down when inspecting secondary mineral formations in (a) Ni-contaminated soils, (b) heazlewoodite–trevorite mineral assemblages, (c) Ni matte, (d) Cu- and Ni-bearing slags, and (e) the silica-rich coatings of the Sudbury area.

McNear et al. (2007) showed for example that the most common weathering products of NiO in limed

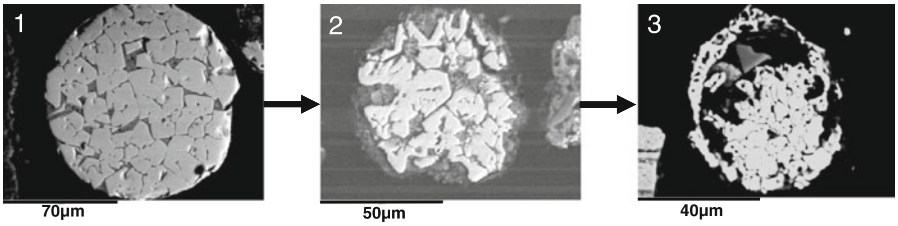

Fig. 12 Proposed weathering sequence (*1*–*3*) for spherical particles with a platy texture of magnetite within a Fe-silicate matrix (see text for details)

(pH=7.5) and unlimed (pH=7) soils near a Ni-refinery in Port Colborne, Canada, were Ni- and Al-hydroxides. These phases, however, were not identified as weathering crusts around NiO and most likely were formed upon mobilization of Ni by organic material (McNear et al. 2007).

Huson and Travis (1961) described in detail the native Ni–heazlewoodite–trevorite mineral assemblage from Mount Clifford, Western Australia. Here, they identified godlevskite [$(Ni, Fe)_7S_6$] as a primary alteration product of heazlewoodite and millerite (NiS) as an alteration product of godlevskite. They also showed that native Ni and trevorite grains were surrounded by rims of Ni-hydroxides and carbonates such as jamborite, [$Ni^{2+}Ni^{3+}$, Co, Fe)$(OH)_2(OH)S$, H_2O] and reevesite [$Ni_6Fe_2^{3+}(CO_3)(OH)_{16}\ (H_2O)_4$].

Dutrizac and Chen (1987) showed that the leaching of a Ni and Cu matte with a $CuSO_4$–H_2SO_4–O_2 solution led to the transformation of heazlewoodite and chalcocite into aqueous Ni^{2+}, polydymite (Ni_3S_4), and covellite (CuS). Further leaching resulted in the formation of Cu- and Ni-sulfates followed by their subsequent dissolution. Similar to the observations above, silicates present in the matte were strongly altered during leaching experiments, whereas Ni and Cu spinels remained largely unaffected.

The formation of secondary phases and the release of trace metals during the weathering of base-metal-bearing slags have been studied in great detail (e.g., Piatak and Seal 2010; Vitkova et al. 2010; Piatak et al. 2004). These studies showed the presence of secondary carbonates, sulfates, and silicates as coatings on altered slag. Identified Cu-bearing phases included malachite, [$Cu_2(CO_3)(OH)_2$], brochantite, [$Cu_4SO_4(OH)_6$], chalcanthite, [$Cu^{2+(}H_2O)_4(SO_4)](H_2O)$, and becherite [$Zn_7Cu^{2+(}OH)_{13}\{SiO(OH)_3\}(SO_4)$].

Mantha et al. (2012) showed that many nanometer-size Cu-bearing particles were dissolved on the atmosphere-coating interface of the silica-rich coatings and resulted in the precipitation of antlerite, $Cu_3(SO_4)(OH)_4$, and guildite, $CuFe^{3+}(SO_4)_2(OH)(H_2O)_4$. These and other sulfates are protected from further weathering by the silica-rich matrix of the coatings. However, their occurrence in the coatings suggests that these phases form initially when Cu-bearing sulfides and oxides are weathered by acidic solutions of high sulfate concentration.

Spherical particles occur in the acidic soils (pH=4–5) and in limed soils (pH~7) of the Greater Sudbury area (Wren 2012). In acidic soils, surface layers of heazlewoodite and bornite may initially transform into godlevskite, polydymite, and covellite. At low activities of $(SO_4)^{2-}$ [i.e., fast removal of $(SO_4)^{2-}$ by pore water], surface layers of Fe–Ni-sulfides convert to hydroxides and, upon, aging into oxides (Fig. 11, step 3a). At higher activities of $(SO_4)^{2-}$, crusts and fillings of secondary sulfates such as brochanite, antlerite, guildite, and chalcanthite may form (step 3b). These Cu-sulfates dissolve (step 4, Fig. 11) and subsequently release Cu, Ni, and $(SO_4)^{2-}$ to the pore water. In limed soils with higher activities of $(CO_3)^{2-}$, Cu- and Ni-bearing carbonates such as reevesite, $Ni_6Fe_2^{3+}(CO_3)(OH)_{16}\ (H_2O)_4$, and malachite, [$Cu_2(CO_3)(OH)_2$], may form weathering crusts around Cu- and Ni-bearing sulfide and oxide inclusions.

4.8 Transformation of Magnetite into Hematite and Release of Cu^{2+} and Ni^{2+}

SEM and optical examinations indicate that areas composed of hematite occur in spherical particles where sulfide inclusions are absent but where fragments of the Fe-silicate matrix remain. The presence of silicate minerals in hematite-bearing spherical particles can be recognized in the Mössbauer spectra of the brown- and red-colored spheres (Fig. 7a, b). These show the presence of unknown Fe^{2+} and Fe^{3+} components with CS and QS values similar to values reported for Fe-silicates (Table 5, McCammon 1995). These observations suggest that the transformation of magnetite into hematite occurs after dissolution of the sulfide inclusions but simultaneously with the alteration of the silicate minerals. The transformation of magnetite into hematite is initiated at the outer rim of the spherical particles where thin layers of hematite form upon oxidation of magnetite (Fig. 7b). These thin layers extend toward the center of the spherical particle with increased weathering (Fig. 7a) until the spherical particles are entirely replaced by hematite (not shown). The Mössbauer spectra indicate that the proportions of magnetite and Fe-silicates decrease in the sequence black → brown → red-colored spheres, whereas the proportions of hematite increase in the same sequence (Fig. 7a–c, Table 5). Hence, the color of a spherical particle can be used to estimate the degrees of alteration of the Fe-silicates and the degree of transformation of magnetite to hematite.

In weathering profiles of mafic rocks, the transformation of magnetite to hematite commonly occurs via the formation of maghemite, γ-Fe_2O_3 (e.g., Santana et al. 2001). However, Mössbauer and Raman analyses do not support the presence of maghemite in the spherical particles. Similarly, studies of weathering profiles (e.g., Santana et al. 2001; Anand and Gilkes 1984; Gilkes and Suddliprakarn 1979) showed the absence of maghemite during the transformation of magnetite into hematite. It is not within the scope of this paper to understand the absence of maghemite in the weathered spherical particles, but the transformations magnetite → maghemite → hematite are obviously complex and depend on many factors such as Eh, pH, weathering rate, trace element content, and crystal size (e.g., Cornell and Schwertmann 1996 and references therein).

Divalent cations such as Co^{2+}, Ni^{2+}, Zn^{2+}, and Cu^{2+} are commonly retained during the transformation of magnetite to maghemite, but are incompatible with the structure of hematite, and migrate toward the surface of the hematite particles during the transformation of magnetite to hematite (Sidhu et al. 1981). This phenomenon may explain why areas composed of hematite are depleted in Cu and Ni relative to magnetite.

4.9 Dissolution Rates of Fe–Cu–Ni Spinels

The weathering sequence of the spherical particles (Fig. 11) indicates that Cu- and Ni-rich sulfide inclusions alter prior to Fe-silicates and oxides. Hence, differences between the weathering rates of the various Cu- and Ni-bearing sulfides are negligible when compared to the weathering rates of silicates and oxides. Consequently, the preferential release of Cu vs. Ni for the smelter-derived particles in the Sudbury soils must be the result of:

(a) The higher dissolution rates of Cu- vs. Ni-bearing oxides
(b) The formation of Ni-bearing oxides during weathering of the Fe–Ni-sulfide inclusions

4.9.1 Dissolution Rates Controlled by Surface Reduction Processes on Cu- and Ni-Bearing Spinels

Anhydrous Cu- and Ni-bearing oxides are commonly the least soluble phases in soils (Alloway 1990), and their dissolution rates can only be measured in strong acidic solutions. For example, Lu and Muir (1987) measured the dissolution rates of $CuFe_2O_4$ and $NiFe_2O_4$ in a 1-M HCl solution. They showed that the dissolution rate of the Cu spinel was 32 times higher than the rate for the Ni spinel and increased to even higher rates under reducing conditions in a Cu^+–HCl solution. X-ray photoelectron spectroscopy (XPS) showed that Cu^+ forms on the surface of $CuFe_2O_4$ under reducing conditions in the gas phase (Faungnawakij et al. 2009) and that the removal rate of Cu-oxide layers by ethyl-alcohol is controlled by the conversion of Cu^{2+} to Cu^+ (Satta et al. 2003).

The results of the XPS measurements suggest that one of the key processes controlling the dissolution rate of $CuFe_2O_4$ is the reduction of Cu^{2+} to Cu^+. Thus, discrepancies in the dissolution rates of $CuFe_2O_4$ and $NiFe_2O_4$ in HCl solutions, with or without Cu^+, may be explained by the following observations: (a) Cu^{2+} can be easily reduced to Cu^+ in reductive solutions (NIAIST 2005); (b) Cu^+ species occur in O-deficient, $CuFe_2O_{4-x}$ spinels (see above); (c) the valence of Cu^+ (weak Lewis acid) is stabilized by the presence of Cl^- (weaker Lewis base than O) through the formation of Cu^+Cl_x complexes in aqueous solution (Stepakova et al. 2006); (d) the linear coordinated Cu^+ is incompatible with the spinel structure; and (e) Ni^{2+} can be reduced to Ni^0 only at extreme reducing conditions, which did not occur during the above described dissolution experiments (i.e., Cu^+ cannot reduce Ni^{2+} to Ni^0; Faure 1998).

The occurrence and formation of Cu^+ species in the structure and on the surface of $CuFe_2O_4$ may also control its dissolution rate. The reduction of Cu^{2+} to Cu^+ in soils is commonly promoted by aldehyde groups, R-COOH (present in polysaccharides), Fe^{2+} and H_2S (Violante et al. 2010; Lowe 1989). Once Cu^+ is released to the soil during weathering, it quickly disproportionates into Cu^{2+}(aq) and Cu(s) (Baker 1990).

4.9.2 Dissolution Rates Controlled by the Grain-Size Distributions of the Cu and Ni Spinels

Chan et al. (1982) showed that the majority of Cu- and Ni-bearing particles emitted from the Copper Cliff smelting center were in the coarse fraction ($d>$ 2.5 μm), whereas Pb–As–S–Se-bearing particles were in the fine fraction ($d<2.5$ μm). However, TEM studies on the silica-rich coatings show that Cu-oxide-bearing nanoparticles are far more common than their Ni-bearing counterparts, suggesting that Cu-bearing phases such as cuprite, cuprospinel, and delafossite occurred and may still occur in a higher proportion in the ultrafine fraction (d<0.1 μm) of the soils.

A decrease in particle size commonly results in an increase in surface area available for dissolution and thus in an increase in the amount of dissolved material (Stumm 1992). Hence, a larger proportion of emitted Cu- vs. Ni-oxide nanoparticles would have resulted in a higher release of Cu into the soils.

4.9.3 Formation of Trevorite During Oxidation of the Sulfides

The occurrence of trevorite in the alteration zone around former sulfide inclusions (Figs. 6d and 11) can be explained by the formation of Ni-bearing Fe-hydroxides and their subsequent transformation to crystalline and thermodynamically more stable minerals (see above). Anhydrous Cu-oxides are not observed around pre-existing sulfide inclusions, indicating that these phases rarely form as secondary alteration products of sulfide minerals. This conclusion is in accord with field and experimental observations that show that Cu-bearing sulfates and carbonates form predominantly as alteration products of Cu-sulfide minerals (see above).

4.10 Emission of Nanoparticles and the Environmental Consequences

Chan et al. (1982) studied the particle size of emitted aerosols by collecting samples above the largest smelter stack in the Sudbury area. The Sudbury soil study (Wren 2012) examined the mineralogical and chemical compositions, as well as the grain-size distributions of particles collected in filters on the largest smelter stack. However, none of these studies examined particles in the nanometer-size range (<1 μm to >10 nm), despite the fact that these particles have (1) the greatest surface area (Gieré and Querol 2010), (2) the longest atmospheric residence time (1–2 weeks) of all particulate matter (Anastasio and Martin 2001), and (3) a significant impact on human health (Pope et al. 2009). For example, airborne nanoparticles containing trace elements such Pb, As, Cu, Ni, and Se can cause serious health effects (e.g., Utsunomiya et al. 2004) due to their toxicity or their occurrence as carcinogens.

Our TEM studies on the silica-rich coatings show that Cu- and Ni-bearing nanoparticles were released by the smelters. The fact that Weinbruch et al. (2002) found nano- to micro-size particles of bunsenite (NiO), trevorite, heazlewoodite, godlevskite, millerite (NiS), and gaspeite ((Ni,Mg,Fe)CO_3) in a working place of a Ni-refinery suggests that Ni- and Cu-bearing nanoparticles are still emitted by smelters, converters, and refining facilities in the Greater Sudbury area.

5 Summary

Copper seems to be more mobile than Ni through its greater presence in the organic and clay fraction of the soils (Wren 2012; Adamo et al. 1996). However, the ratios of Cu and Ni in emissions from smelters in the Greater Sudbury area and those present in the soil are close to 1, indicating that any differences in the mobility of these elements are small. The larger proportions of Cu in these low T phases can be explained by the formation of stronger adsorption complexes between Cu and the corresponding surface species and with the preferential release of Cu vs. Ni by smelter-derived particles. The latter explanation was verified in this study through examination of the chemical and mineralogical compositions of smelter-derived spherical particles in soils and silica-rich rock coatings. It has been shown specifically that the particles are composed mainly of magnetite and Fe-silicates with minor Cu- and Ni-bearing phases such as heazlewoodite, bornite, Cu- and Ni-rich spinels, delafossite, and cuprite or tenorite. Examination of weathered spherical particles in soils and nanometer-size particles in silica-rich rock coatings indicate that the preferential release of Cu vs. Ni to the clay and organic fractions of the soils is most likely a product of the higher dissolution rate of the Cu vs. Ni spinels, a higher proportion of soluble Cu-oxide particles in the finer fraction of the emitted particles, and the formation of low solubility Ni spinel phases as secondary products around sulfide inclusions.

Acknowledgments This work was supported by NSERC Discovery grants to MS, AMcD, and FCH; NSERC summer student scholarships to SL and KS; and an Ontario Graduate Scholarship to NM. MH acknowledges NSF and EPA under NSF Cooperative Agreement EF-0830093. Any opinions, findings, conclusions, or recommendations expressed in this material are those of the authors and do not necessarily reflect the views of the NSF or the EPA. This work has not been subjected to EPA review and no official endorsement should be inferred. We would like to thank the technical staff members at the Central Analytical Facility, Laurentian University and at the Nanoscale Characterization and Fabrication Laboratory, ICTAS, Virginia Tech, for their assistance.

References

Adamo, P., Dudka, S., Wilson, M. J., & McHardy, W. J. (1996). Chemical and mineralogical forms of Cu and Ni in contaminated soils from the Sudbury mining and smelting region. *Canada. Environ. Pollut., 91*, 11–19.

Ahlawat, A., & Sathe, V. G. (2010). Raman study of $NiFe_2O_4$ nanoparticles, bulks and films: Effect of laser power. *J. Raman Spectroscopy., 42*, 1087–1094.

Alloway B.J.(1990) Soil processes and the behaviour of metals. In B.J. Alloway (Ed.), Heavy metals in soils. New York: Wiley, 339. p.7-28.

Anand, R. R., & Gilkes, R. J. (1984). Mineralogical and chemical properties of weathered magnetite grains from lateritic saprolite. *J. Soil Science., 35*, 559–567.

Anastasio, C., & Martin, S. T. (2001). Atmospheric nanoparticles. *Reviews in Mineralogy and Geochemistry, 44*, 293–349.

Baker D.E. (1990) Copper metals in soils. In B.J. Alloway (Ed.), Heavy metals in soils. New York: Wiley, 339. p.151-176.

Bao, H. M., & Reheis, M. C. (2003). Multiple oxygen and sulfur isotopic analyses on water-soluble sulfate in bulk atmospheric deposition from the southwestern United States. *J. Geophysi. Res., 108*, 4430–4438.

Batonneau, Y., Bremard, C., Gegembre, L., Laureyns, J., LeMaguer, A., LeMaguer, D., Perdrix, E., & Sobanska, S. (2004). Speciation of PM sources of airborne nonferrous metals within the 3-km zone of lead/zinc smelters. *Environmental Science and Technology, 38*, 5281–5289.

Brock, C. A., Hamill, P., Wilson, J. C., Jonsson, H. H., & Chan, K. R. (1995). Particle formation in the upper tropical troposphere—A source of nuclei for the stratospheric aerosol. *Science, 270*, 1650–1653.

Campbell, J. L., McDonald, A. M., Perrett, G. M., & Taylor, S. M. (2011). A GUPIX-based approach to interpreting the PIXE-plus-XRF spectra from the Mars Exploration rovers: II geochemical reference materials. *Nuclear InstrumMethods in Phys. Res. Sec B., 269*, 69–81.

Chan W.H., Lusis M.A., Vet R., and Skelton B.G. (1982) Size distribution and emission rate measurements of particulates in the Inco 381 m chimney and iron ore recovery plant stack fumes, 1979–80. Sudbury Environmental Study, Ontario Ministry of Environment. p.101.

Cheng, Z., Abernathy, H., & Liu, M. (2007). Raman spectroscopy of nickel sulfide Ni3S2. *Phys. Chem. C, 111*, 17997–18000.

Connolly, H. C., & Hewins, R. H. (1995). Chondrules as products of dust collisions with totally molten droplets within a dust-rich nebular environment: An experimental investigation. *Geochim. Cosmochim., 59*, 3231–3246.

Cornell, R. M., Schneider, W., & Giovanoli, R. (1992). The effect of nickel on the conversion of amorphous iron(III) hydroxide into more crystalline iron oxides in alkaline media. *J. Chem. Tech. Biot., 53*, 73–79.

Cornell R.M. and Schwertmann U. (1996) The iron oxides. Structure, properties, reactions, occurrences and uses. New York: VCH Verlagsgesellschaft.

Davies, B. E. (1983). Heavy metal contamination from base metal mining and smelting: Implications for man and his environment. *Appl. Environ. Geochem., 1*, 425–462.

De Faria, D. L. A., Silva, S. V., & De Oliveira, M. T. (1997). Raman microspectroscopy of some iron oxide and oxyhydroxides. *J. Raman Spectroscopy., 28*, 873–878.

Dollase, W. A. (1986). Correction of intensities for preferred orientation in powder diffractometry: Application of the March model. *Journal of Applied Crystallography, 19*, 267–272.

Dutrizac, J. E., & Chen, T. T. (1987). A mineralogical study of the phases formed during the $CuSO_4$–H_2SO_4–O_2 leaching of nickel-copper matte. *Can. Metallurg. Quart., 26*, 265–276.

Dural, J. (2009). Thermal instability of the tetragonally distorted structure of copper–iron materials. *Z. Kristallogr. Suppl., 30*, 335–340.

Durocher, J., & Schindler, M. (2011). Iron-hydroxide, iron-sulfate and hydrous silica coatings in acid-mine tailings facilities: A comparative study of their trace-element composition. *Applied Geochem., 26*, 1337–1352.

Ertseva, L. N., Korotkova, O. V., Seregin, P. S., & Fokeeva, I. G. (2003). Distribution of micro-impurities among phases of converter and matte from Pechenganikel's combine. *Russ. J. Applied Chem., 76*, 884–887.

Evans J.P., Mackey P.J., and Scott J.D.(1991) Smelter gas cleaning. Impact of gas cooling techniques on smelter dust segregation. In T.J.A. Smith and C.J. Newman (Eds.), Smelter process gas handling and treatment (p. 135-145). Metals and Materials Society, Warrendale.

Faungnawakij, K., Shimoda, N., Fukunaga, T., Kikuchi, R., & Eguchi, K. (2009). Crystal structure and surface species of $CuFe_2O_4$ spinel catalysts in steam reforming of dimethyl ether. Appl. *Catalysis B: Environ. 92*, 341–350.

Faure, G. (1998). *Principles and applications of geochemistry* (2nd ed., p. 600p). New Jersey: Prentice-Hall.

Freedman, B., & Hutchinson, T. C. (1980). Pollutant inputs from the atmosphere and accumulations in soils and vegetation near a nickel-copper smelter at Sudbury, Ontario, Canada. *Canadian Journal of Botany, 58*, 108–132.

Gieré, R., & Querol, X. (2010). Solid particulate matter in the atmosphere. *Elements., 6*, 215–222.

Gilkes, R. J., & Suddliprakarn, A. (1979). Magnetite alteration in deeply weathered adamelite. *J. Soil Science., 30*, 357–361.

Gbor, P. K., Ahmed, I. B., & Jia, C. Q. (2000). Behaviour of Co and Ni during aqueous sulphur dioxide leaching of nickel smelter slag. *Hydrometallurgy, 57*, 13–22.

Gregurek, D., Reimann, C., & Stumplf, E. F. (1998). Mineralogical fingerprints of industrial emissions—an example from Ni mining and smelting on the Kola Peninsula, NW Russia. *Science Total Environ., 221*, 189–200.

Gregurek, D., Melcher, F., Pavlov, V. A., Reimann, C., & Stumpfl, E. F. (1999). Mineralogy and mineral chemistry of snow filter residues in the vicinity of the nickel–copper processing industry, Kola Peninsula, NW Russia. *Mineralogy and Petrology, 65*, 87–111.

Hamill, P., Jensen, E. J., Russell, P. B., & Bauman, J. J. (1997). The life cycle of stratospheric aerosol particles. *Bull. Am. Meteor. Soc., 78*, 1395–1410.

Henderson, P. J., McMartin, L., Hall, G. E., Percival, J. B., & Walker, D. A. (1998). The chemical and physical characteristics of heavy metals in humus and till in the vicinity of the base metal smelter at FlinFlon, Manitoba, Canada. *Environ. Geolog., 34*, 39–58.

Hogan, G. D., & Wotton, D. L. (1984). Pollutant distribution and effects on forests adjacent to smelters. *Journal of Environmental Quality, 13*, 377–382.

Huson, D. R., & Travis, G. A. (1961). A native nickel–heazlewoodite–ferroantrevorite assemblage from Mount Clifford, Western Australia. *Economic Geology, 76*, 1686–1697.

Hutchinson, T. C., & Whitby, L. M. (1974). Heavy-metal pollution in the Sudbury mining and smelting region of Canada, I. Soil and vegetation contamination by nickel, copper, and other metals. *Environmental Conservation, 1*, 123–131.

Jackson, T. A. (1978). The biogeochemistry of heavy metals in polluted lakes and streams at FlinFlon, Canada, and a proposed method for limiting heavy-metal pollution of natural waters. *Environmental Geology, 2*, 173–189.

Kalkstein, L. S., & Greene, J. S. (1997). An evaluation of climate/mortality relationships in large U.S. cities and the possible impacts of a climate change. *Environmental Health Perspectives, 105*, 84–93.

Kirkpatrick, R. J. (1975). Crystal growth from the melt—a review. *American Mineralogist, 60*, 798–814.

Kliza, D. A., Telmer, K. T., Bonham-Carter, G. F., Hall, G. E. M. (2000). Geochemistry of snow from the Rouyn-Noranda region of western Quebec: An environmental database. Open File, 3869.

Knight, R. D., & Henderson, P. J. (2006). Smelter dust in humus around Rouyn-Noranda, Quebec. *Geochem. Exploit. Environ. Analys., 6*, 203–214.

Knight R.D., and Henderson P.J. (2005) Characterization of smelter dust from the mineral fraction of humus collected around Rouyn-Noranda, Quebec. In G. Bonham-Carter (Ed.) Metals in the environment around smelters at Rouyn-Noranda, Quebec, and Belledune, New Brunswick: Results and conclusions of the GSC-MITE Point Sources Project. Bulletin, 584. Geological Survey of Canada.

Lastra-Quintero, R. (1998). Characterization and separation of a copper smelter dust residue. *Can. Metallurg. Quarterly., 26*, 85–90.

Lofgren, G. (1974). An experimental study of plagioclase morphology. *American Journal of Science, 264*, 243–273.

Lowe, L. E. (1989). Carbohydrates in soil. In M. Schnitzer & S. U. Khan (Eds.), *Soil Organic matter* (pp. 65–69). New York: Elsevier.

Lu, Z., & Muir, D. M. (1987). Dissolution of metal ferrites and iron oxides by HCl under oxidizing and reducing conditions. *Hydrometallurgy, 21*, 9–21.

Mantha, N. M., Schindler, M., Murayama, M., Hochella, M. F. Jr. (2012) Silica- and sulfate-bearing rock coatings in smelter areas: Products of chemical weathering and atmospheric pollution I. Formation and mineralogical composition. *Geochim. Cosmochim. Acta.* doi: doi:10.1016/j.gca.2012.01.033

Mantha N. and Schindler M. (2012) Silica- and sulfate-bearing rock coatings in smelter areas: Products of chemical weathering and atmospheric pollution. II. Metal and Metalloid composition. *Geochim. Cosmochim.* (in press)

McCammon, C. (1995). *Mössbauer spectroscopy of minerals. Mineral physics and crystallography. A handbook of physical constants*. Washington: AGU.

McNear, D. H., Jr., Chaney, R. L., & Sparks, D. L. (2007). The effects of soil type and chemical treatment on nickel speciation in refinery enriched soils: A multi-technique investigation Geochim. *Cosmochim. Acta., 71*, 2190–2208.

Morris, R. V., Kligelhöfer, G., Bernhardt, B., Schröder, C., Radionov, D. S., de Souza Jr, P. A., Yen, A., Gellert, R., Evlanov, E. N., Foh, K. E., Gütlich, P., Ming, D. W., Fenz, F., Wdowiak, T., Squyres, S. W., & Arvidson, R. E. (2004). Mineralogy at Gusev Crater from the Mössbauer spectrometer on the Spirit rover. *Science, 305*, 833–836.

National Institute of Advanced Industrial Science and Technology (NIAIST) (2005). Atlas of Eh-pH diagrams, Intercomparison of thermodynamic databases. In N. Takeno (Ed.), Geological Survey of Japan Open File Report No.419, 1–287.

Norman, A. L., Belzer, W., & Barrie, L. A. (2004). Insights into the biogenic contribution to total sulphate in aerosol and precipitation in the Fraser Valley afforded by isotopes of sulphur and oxygen. *Journal of Geophysical Research, 109*, 5311–5320.

Nriagu, J. O., & Wong, H. K. (1983). Selenium pollution of lakes near the smelters at Sudbury, Ontario. (1983). *Nature, 301*, 55–57.

Ozvacic V. (1982) Emissions of sulphur oxides, particulates and trace elements in the Sudbury basin. Ontario Ministry of Environment report SES 008/82, pp. 82.

Pavunny S.P., Kumar A., Katiyar R.S. (2010) Raman spectroscopy and field emission characterization of delafossite $CuFeO_2$. Journal of Applied Physics. 107, 013522(1-7).

Tan, P., & Zhang, C. (1997). Thermodynamic analysis of nickel smelting Process. *Journal of Central South University of Technology, 4*, 84–88.

Piatak, N. M., Seal, R. R. I. I., & Hammarstrom, J. M. (2004). Mineralogical and geochemical controls on the release of trace elements from slag produced by base- and precious-metal smelting at abandoned mine sites. *Applied Geochemistry, 19*, 1039–1064.

Piatak, N. M., & Seal, R. R., II. (2010). Mineralogy and the release of trace elements from slag from the Hegeler Zinc smelter, Illinois (USA). *Applied Geochemistry, 25*, 302–320.

Pope, C. A., Ezzati, M., & Dockery, D. W. (2009). Fine-particulate air pollution and life expectancy in the United States. *The New England Journal of Medicine, 360*, 376–386.

Samuelsson, C., & Bjorkman, B. (1998). Dust forming mechanisms in the gas cleaning system after the copper converting process. (I) Sampling and characterization. *Scand. J. Metallurg., 27*, 54–63.

Santana, G. P., Fabris, J. D., Goulart, A. T., & Santana, D. P. (2001). Magnetite and its transformation to hematite in a soil derived from steatite. *R. Bras. Ci. Solo., 25*, 33–42.

Satta, A., Shamiryan, D., Baklanov, M. R., Whelan, C. M., Quoc, T. L., Beyer, G. P., Vantomme, A., & Maex, K. (2003). The removal of copper oxides by ethyl alcohol monitored in situ by spectroscopic ellipsometry. *Journal of the Electrochemical Society, 150*, 300–306.

Schindler, M., Durocher, J., Abdu, Y., & Hawthorne, F. C. (2009). Hydrous silica coatings: Occurrence, speciation of metals and environmental significance. *Environ. Science Tech., 43*, 8775–8780.

Schindler, M., Fayek, M., & Hawthorne, F. C. (2010). Uranium in opaline rock-coatings at the Uranium Ore Deposit Nopal 1, Pena Blanca, Mexico: Indications for the uptake and retardation of radionuclides. *Geochim. Cosmochim., 74*, 187–202.

Sidhu, P. S., Gilkes, R. J., & Posner, A. M. (1981). Oxidation and ejection of nickel and zinc from natural and synthetic magnetites. *Soil Science Society of America Journal, 45*, 641–644.

Stepakova, L.V., Skirpkin, M. Yu., Korneeva, V.V., Grigoriev, Ya. M. and Burkov, K.A. (2006) Effect of the oxidation state of copper on the solution-solid phase equilibria in $CuCl_x$–MCl–H2O systems. Rus. J. Gen. Chem. 76,512-516.

Stumm, W. (1992). *Chemistry of the solid–water interface* (p. 428). New York: Wiley.

Tang, X. X., Manthiram, A., & Goodenough, J. B. (1989). Copper ferrite revisited. *J. Solid State Chem., 79*, 250–262.

Thyse, E. L., Akdogan, G., Taskined, P., & Eksteen, J. J. (2011). The distribution of metallic elements in granulated nickel converter matte phase. *South African Pyrometallurgy, 2011* (1), 173–184.

Utsunomiya, S., Jensen, K. A., Keeler, G. J., & Ewing, R. C. (2004). Direct identification of trace metals in fine and ultra-fine particles in the Detroit urban atmosphere. *Environmental Science and Technology, 38*, 2289–2297.

Violante, A., Cozzolino, V., Perelomov, L., Caporale, A. G., & Pigna, M. (2010). Mobility and bioavailability of heavy metals and metalloids in soil environments. *J. Soil. Sci. Plant. Nutr., 10*, 268–292.

Vitkova, M., Ettler, V., Kribek, B., Sebek, O., & Mihaljevic, M. (2010). Primary and secondary phases in copper–cobalt smelting slags from the Copperbelt Province Zambia. *Mineralogical Magazine, 74*, 581–600.

Wang, J. H., Cheng, Z., Bredas, J. L., & Liu, M. (2007). Electronic and vibrational properties of nickel sulfides from first principles. *Journal of Chemical Physics, 127*, 214705-1–214705-8.

Weinbruch, S., Van Aken, P., Ebert, M., Thomassen, Y., Skogstad, A., Chashchin, V. P., & Nikonov, A. (2002). The heterogeneous composition of working place aerosols in a nickel refinery: A transmission and scanning electron microscope study. *Journal of Environmental Monitoring, 4*, 344–350.

Whitby, L. M., Stokes, P. M., Hutchinson, T. C., & Myslik, G. (1976). Ecological consequence of acidic and heavy-metal discharges from the Sudbury smelters. *The Canadian Mineralogist, 14*, 47–57.

Wren, C. (2012). Risk assessment and environmental management: A case study in Sudbury, Ontario, Canada. *Progress in Environmental Science, Technology and Management, 1*, 1–450.

Zoltai, S. (1988). Distribution of base metals in peat near a smelter at FlinFlon. Manitoba. *Water, Air, and Soil Pollution, 37*, 217–228.